Available online at www.sciencedirect.com
ScienceDirect
Icarus ••• (••••) •••–•••
ICARUS
www.elsevier.com/locate/icarus

Saturn's dynamic D ring

Matthew M. Hedman [a,*], Joseph A. Burns [a,b], Mark R. Showalter [c], Carolyn C. Porco [d], Philip D. Nicholson [a], Amanda S. Bosh [e], Matthew S. Tiscareno [a], Robert H. Brown [f], Bonnie J. Buratti [g], Kevin H. Baines [g], Roger Clark [h]

[a] *Department of Astronomy, Cornell University, Ithaca, NY 14853, USA*
[b] *Department of Theoretical and Applied Mechanics, Cornell University, Ithaca, NY 14853, USA*
[c] *SETI Institute, Mountain View, CA 94043, USA*
[d] *CICLOPS, Space Science Institute, Boulder, CO 80301, USA*
[e] *Boston University at Lowell Observatory, Flagstaff, AZ 86001, USA*
[f] *Lunar and Planetary Lab, University of Arizona, Tucson, AZ 85721, USA*
[g] *JPL, 4800 Oak Grove Drive, Pasadena, CA 91109, USA*
[h] *USGS, Mail Stop 964, P.O. Box 25046, Federal Center, Denver, CO 80225, USA*

Received 2 June 2006; revised 7 November 2006

Abstract

The Cassini spacecraft has provided the first clear images of the D ring since the Voyager missions. These observations show that the structure of the D ring has undergone significant changes over the last 25 years. The brightest of the three ringlets seen in the Voyager images (named D72), has transformed from a narrow, <40-km wide ringlet to a much broader and more diffuse 250-km wide feature. In addition, its center of light has shifted inwards by over 200 km relative to other features in the D ring. Cassini also finds that the locations of other narrow features in the D ring and the structure of the diffuse material in the D ring differ from those measured by Voyager. Furthermore, Cassini has detected additional ringlets and structures in the D ring that were not observed by Voyager. These include a sheet of material just interior to the inner edge of the C ring that is only observable at phase angles below about 60°. New photometric and spectroscopic data from the ISS (Imaging Science Subsystem) and VIMS (Visual and Infrared Mapping Spectrometer) instruments onboard Cassini show the D ring contains a variety of different particle populations with typical particle sizes ranging from 1 to 100 microns. High-resolution images reveal fine-scale structures in the D ring that appear to be variable in time and/or longitude. Particularly interesting is a remarkably regular, periodic structure with a wavelength of ∼30 km extending between orbital radii of 73,200 and 74,000 km. A similar structure was previously observed in 1995 during the occultation of the star GSC5249-01240, at which time it had a wavelength of ∼60 km. We interpret this structure as a periodic vertical corrugation in the D ring produced by differential nodal regression of an initially inclined ring. We speculate that this structure may have formed in response to an impact with a comet or meteoroid in early 1984.

Keywords: Planetary rings; Saturn, rings

1. Introduction

The D ring is the innermost component of Saturn's ring system. As such, it resides in a region where Saturn's tides and higher-order gravity moments are more important than elsewhere and close to a newly discovered radiation belt (Krimigis et al., 2005). The D-ring particles therefore occupy an extreme environment, and accordingly the dynamics of D-ring material may test the limits of applicability of current models of the rings.

The D-ring's location near the planet, combined with its low optical depth, makes it nearly impossible to observe directly from Earth. Using images taken in 1969, Guérin (1973) reported a detection of material interior to the C ring around 70,000 km from the center of Saturn, but in 1979 Pioneer 11

* Corresponding author.
E-mail address: mmhedman@astro.cornell.edu (M.M. Hedman).

0019-1035/$ – see front matter
doi:10.1016/j.icarus.2006.11.017

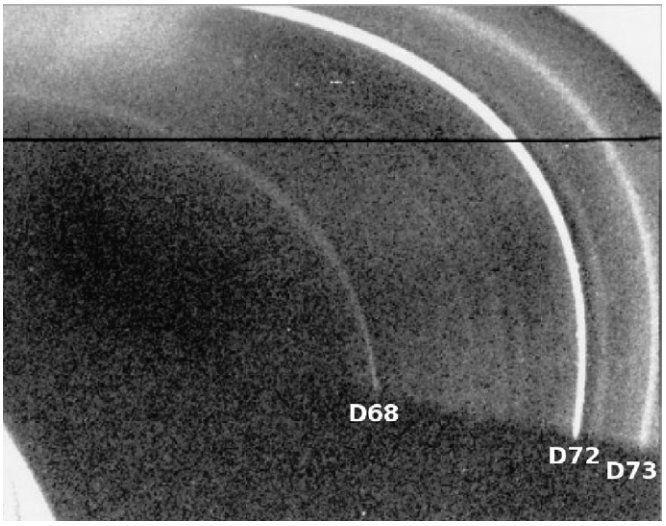

Fig. 1. Image of the D ring taken by Voyager 1 (image number 34946.50, phase angle 156°, resolution 15 km/pixel). The C-ring's overexposed edge is visible in the upper right-hand corner of the image, while the planet's overexposed limb is visible in the lower left-hand corner of the image. The planet's shadow extends across the lower part of the image. The three brightest bands correspond to D68, D72 and D73. The horizontal black line is a data drop-out. A radial brightness profile derived from this image is provided in Fig. 4.

did not observe any material in this region (Gehrels et al., 1980). Subsequent Voyager observations did reveal structures interior to the C ring, but they were much too faint to be consistent with the previous ground-based observations. If we exclude these early data, all of the information about the structure and composition of the D ring prior to Cassini comes from the Voyager missions and a single ground-based occultation. The occultation data were presented in Bosh and Olkin (1996), while the eleven Voyager images of the D ring were described first by Marley and Porco (1993) and in more detail by Showalter (1996). In the images, the D ring appeared as a diffuse sheet of material plus three ringlets centered at 67,580, 71,710 and 73,145 km from Saturn's center, which were named D68, D72 and D73, respectively (Showalter, 1996). The best Voyager image is reproduced here in Fig. 1, while two radial brightness profiles from Voyager images are plotted in Fig. 4. D68 and D72 were narrow features near the resolution limit of the Voyager cameras (∼15 km/pixel), while D73 was broader (roughly 200 km FWHM). D72 was the brightest ringlet and exhibited a strong forward-scattering peak, implying that it was composed primarily of small particles. Phase and color information on the rest of the D ring was limited, but the low brightness and optical depth of this region suggested that the entire ring was also made up of small particles (Burns et al., 2001).

Now, twenty-five years later, we are again able to observe the D ring in detail thanks to the Cassini spacecraft in orbit around Saturn. During its first two years (28 orbits) around the planet, Cassini imaged the D ring over a wide range of geometries with much better signal-to-noise than the Voyagers and with resolutions as good as 2 km/pixel. These new observations reveal that the D ring has very complex structures on a wide range of scales and contains a variety of distinct particle populations. Furthermore, the D ring has changed dramatically since the Voyager missions; there is even evidence that some structures in this region have continued to evolve over the first half of the nominal Cassini mission.

This report summarizes our current state of knowledge of the D ring, beginning with a summary of how the Cassini data were processed. Then we provide an overview the basic D-ring structure observed by Cassini, how this compares with the Voyager data, and how it depends on the observing geometry. This is followed by some preliminary remarks on the photometric and spectral properties of this ring, focusing on the material visible at high phase angles. We then turn to a detailed survey of the D-ring's structure, with special emphasis on features that appear to be variable in time or longitude. The processes responsible for shaping many parts of the D ring are still obscure and require further investigation. However, a region between 73,200 and 74,000 km contains a periodic 30-km wave-like pattern that we interpret as a vertical corrugation that may have arisen from a close encounter between a comet or meteoroid and the inner rings in 1984.

2. Cassini data processing

The Cassini data presented here come from the Imaging Science Subsystem (ISS) and the Visual and Infrared Mapping Spectrometer (VIMS) instruments. ISS consists of a Narrow-Angle Camera (NAC) and a Wide-Angle Camera (WAC), which produce 1024 × 1024 pixel images with pixel resolutions of 6 and 60 μrad, respectively. Both cameras are equipped with multiple filters, but nearly all the images used in this paper were taken with the clear filters, which have effective central wavelengths of 650 nm (NAC) and 611 nm (WAC) (Porco et al., 2004). VIMS obtains spatially resolved spectra at visual and infrared wavelengths (0.35 to 5.1 microns) with a spectral resolution of roughly 0.016 microns in the infrared and a spatial resolution of 0.5 mrad (Brown et al., 2004).

2.1. Calibration

The raw data from both instruments are calibrated with the standard pipelines described in Porco et al. (2004) and McCord et al. (2004). These pipelines remove backgrounds, perform standard flatfielding procedures, and convert the instrument's data numbers into I/F, a measure of reflectance which equals unity for a perfect Lambert surface oriented normal to the incident sunlight. To account for variations in viewing geometry, the observed I/F values were converted to "normal I/F" $= \mu \times I/F$, where μ the cosine of the emission angle (derived from the observation geometry). The normal I/F of the rings should be independent of emission angle so long as $\tau/\mu \ll 1$ (where τ is the ring's normal optical depth), which is true for all the D-ring images. All of the radial profiles presented below are given in terms of normal I/F; however, we caution that the absolute calibrations of the instruments have not yet been completely validated by comparisons with ground-based and Hubble Space Telescope measurements.

2.2. Geometrical navigation and radial scans

Both the ISS and VIMS data were geometrically navigated using the appropriate spacecraft and trajectory SPICE kernels. For each observation, this rough pointing was confirmed or refined using a combination of background stars and the C-ring's inner edge, which was assumed to be located at a radius of 74,490 km (French et al., 1993). After the images were pointed, the signal was azimuthally averaged to obtain radial profiles of brightness and spectra. Error bars on these profiles were computed based on the scatter of the data points within each radial bin. The error bars are included in the plots of VIMS spectra, but the ISS images described here have sufficient signal-to-noise that the uncertainties in the radial structure due to counting statistics are below 10^{-6} in I/F per resolution-width radial bin for the exposure durations of 1 s typically used for D-ring images. These uncertainties are typically comparable to the thicknesses of the lines, so statistical error bars are not included in most of these brightness profiles.

After obtaining the radial profiles, we further refined the pointing of the ISS data by comparing the locations of features in the innermost 500 km of the C ring among the different profiles. These features all aligned to within 1–2 km in the profiles derived from high-resolution images and images pointed using stars. However, lower-resolution images navigated primarily with the C-ring's inner edge could be systematically shifted in radius by as much as 20 km. These shifts arise because the inner edge of the C ring is not a simple step function in I/F. Instead, the innermost 200 km of the C ring consists of a series of narrow ringlets, so the apparent position of the edge (defined as the point of maximum slope) depends on the resolution, phase angle and signal-to-noise of the image. Since, to first order, this effect produces only an overall offset in radial scale, we simply shifted the radii of the relevant scans by constant amounts to bring the C-ring features into alignment with the profiles derived from the high-resolution images.

2.3. Comment on instrumental artifacts

The D-ring's low surface brightness and its proximity to both Saturn and the main rings mean that instrumental artifacts such as stray light signals can potentially produce significant contamination. Efforts to quantify these spurious signals and to cross-calibrate the various Cassini instruments are still ongoing. In this paper, we report on data for which these instrumental artifacts can be largely ignored.

The spurious patterns due to instrumental artifacts are either smooth compared to the real D-ring structure or not aligned with ring features, so they do not produce significant errors in radial brightness profiles beyond a slowly varying background. In high-phase images where the main rings and the planet are comparatively dark, the background can be well approximated as a constant offset, while in low-phase images a low-order polynomial is sometimes required. In either case, the background does not significantly affect analyses of the detailed structure of the D ring.

By contrast, even smooth background variations can significantly contaminate spectroscopic and photometric measurements. We therefore must postpone a full analysis of the D-ring's photometric properties until more sophisticated background subtraction techniques are developed. However, Cassini has performed several extremely high-phase observations of the D ring, where backgrounds are exceptionally low and the D ring itself is exceptionally bright. These data enable us to perform some preliminary studies of the photometry and spectra of the D-ring's forward-scattering component (see Section 4).

3. Overview

Figs. 1, 2 and 4 provide global views of the D ring from high-phase-angle images taken by Voyager and Cassini. The Cassini profile contains three peaks that occur at locations similar to the three main ringlets seen in the Voyager profiles. These features can be reasonably identified with D68, D72 and D73 (Showalter, 1996). However, whereas D72 was a bright, narrow ringlet in the Voyager images, it now appears to be a broader and fainter feature, whose center of light has shifted substantially inwards relative to other D-ring features. These are the largest secular changes in the entire Saturn ring system observed thus far. It is even possible that the feature called D72 in the Voyager images has disappeared completely, and the ringlet observed today is a separate entity, perhaps identifiable with the shallow ramp seen interior to D72 in the Voyager 1 profile in Fig. 4. Despite this ambiguity in the relationship between the

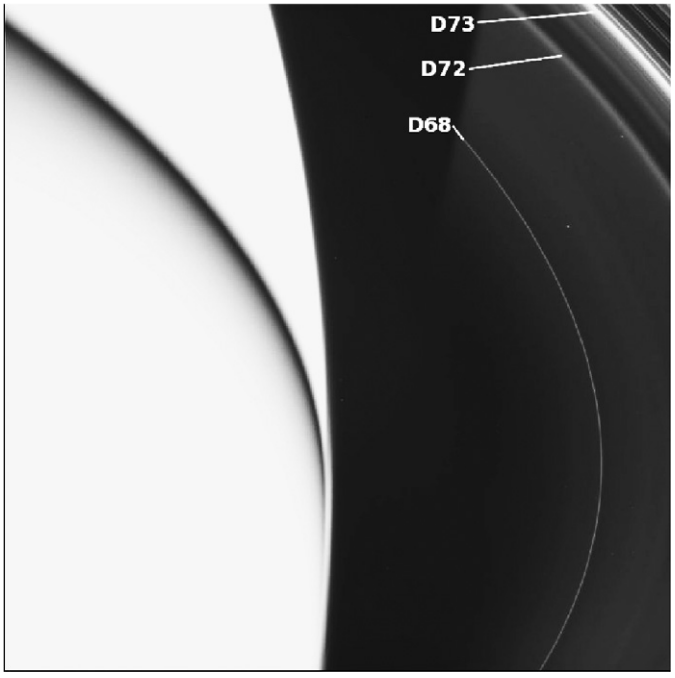

Fig. 2. Image of the D ring taken by the Wide-Angle Camera on Cassini (W1500088644) at a phase angle of 171° with an exposure duration of 3.2 s and a resolution of 17 km/pixel. The inner edge of the C ring lies at the upper right-hand corner of the image. The planet occupies the left half of the image, and its shadow extends vertically along the middle upper part of the image. The three ringlets D68, D72 and D73 are labeled. A radial brightness profile derived from this image is presented in Fig. 4.

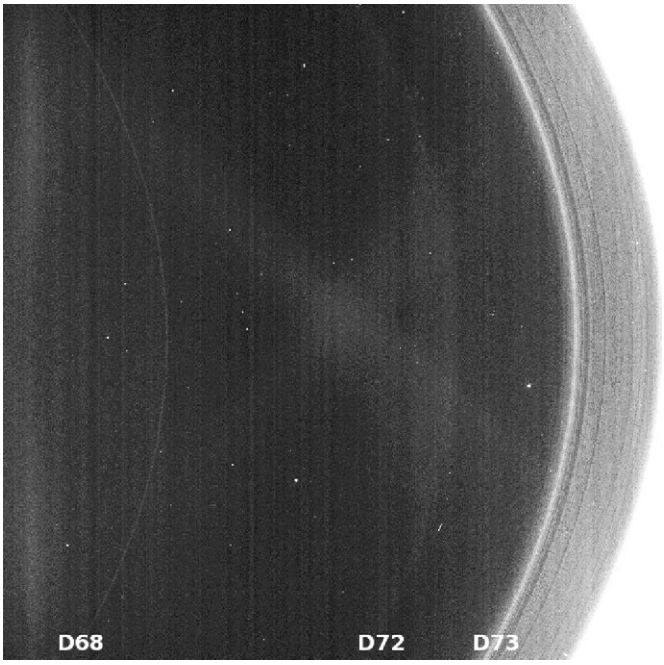

Fig. 3. Image of the D ring taken by the Narrow-Angle Camera on Cassini (N1493559711) at a phase angle of 38° with an exposure duration of 2 s and a resolution of 7 km/pixel. This image has been rotated 90° counterclockwise so the rings are oriented like they are in previous images. The overexposed inner part of the C ring lies at the right side of the image. The faint diagonal streaks across the image center and the vertical banding (which is horizontal in the original image) are instrumental artifacts (Porco et al., 2004). D73's location is marked by the relatively bright inner edge of the band extending inwards from the C ring. D68 can be seen to the left, and D72 appears very faintly near the center of the image. A radial brightness profile derived from this image is shown in Fig. 4.

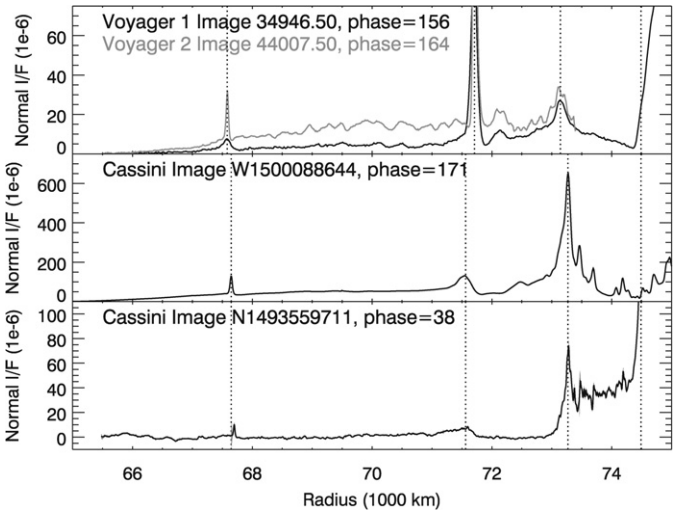

Fig. 4. Comparison of the D ring's morphology at high phase angles observed by Voyager (top) and Cassini (middle), along with the D-ring structure at low phase angles seen by Cassini (bottom). The Voyager profiles come from images taken at 15 km/pixel resolution, one of which is shown in Fig. 1. The high-phase Cassini profile comes from the image shown in Fig. 2, which has a resolution of 17 km/pixel and exposure duration of 3.2 s. Although both profiles are based on images taken through each spacecraft's clear filters, differences in the filter functions between the instruments and the somewhat higher phase angle of the Cassini observation mean that the absolute I/F values are not directly comparable. The low-phase profile comes from the image shown in Fig. 3 and has a resolution of 7 km/pixel and an exposure duration of 2 s. Small spikes due to cosmic rays and stars, as well as a background quadratic due to stray light gradients have been removed from this profile for display purposes only. Dotted lines mark the nominal positions of the three named ringlets in the profiles and the position of the C ring's inner edge (at right).

features observed by Voyager and Cassini, we will henceforth refer to the ringlet observed in the Cassini profiles as D72, with the caveat that it may not be directly related with the Voyagers' D72.

In addition to the dramatic changes in D72's shape, the Cassini profiles differ from the Voyager ones in a number of more subtle ways. The Cassini data indicate that the peaks of all three ringlets are displaced from previously reported values. The average radial locations of D68, D72 and D73 are now 67,650, 71,560 and 73,270 km; +70, −150 and +120 km, respectively, from the radii measured (with an uncertainty of order 10 km) in Voyager images by Showalter (1996). Except for D68 (discussed below), the positions of these features are the same in all available Cassini images, so these differences cannot be ascribed to eccentricities or inclinations. The inward displacement of D72 is significant regardless of whether we use the Marley and Porco (1993) or the Showalter (1996) values for the position of this feature during the Voyager encounters. D73 and D68 are also displaced outward significantly relative to the positions reported in Showalter (1996) (these displacements are not significant compared with the Marley and Porco (1993) estimates, which have 3–4 times larger error bars). All three ringlets have therefore apparently shifted relative to each other over the last twenty-five years.

The Voyager observations detected a diffuse sheet of material between D68 and D73 which had quasi-sinusoidal brightness variations with a typical wavelength of ∼500 km. High-phase images taken by Cassini also show this diffuse material as a region of enhanced brightness exterior to 65,000 km (which is not clearly visible in low-phase images), but the periodic brightness variations are much more muted, and have only been seen unambiguously in one sequence at very high phase (see Figs. 2 and 9 and Section 5.1.1 below).

The region surrounding D73 is more complex in the high-phase Cassini profile than it is in the comparable Voyager data (this zone was not covered particularly well in the Voyager images). To fully appreciate this region's structure, however, it needs to be viewed at both high and low phase angles. As shown in Figs. 2–4, the three main ringlets can be observed at both high and low phase angles, while the diffuse material between D73 and D68 is almost invisible at low phase angles, implying small particles. However, between D73 and the C-ring edge, where the high-phase data show a series of discrete ringlets, the low-phase images show a continuous sheet of material with a series of dips or notches. The two strongest dips in this sheet (at 73,450 and 73,700 km) observed at low phase correlate with the two strongest peaks seen at high phase. As we will describe in Sections 5.2.2 and 6 below, this portion of the D ring contains abundant and perplexing fine-scale structure.

Given the variable appearance of the D ring in time and phase angle, we will avoid naming structures as much as possi-

ble. However, we find it is useful to divide the D ring into two parts: the "inner D ring" which contains all the material interior to 72,000 km; and the "outer D ring" which consists of the region between 72,000 km and the inner edge of the C ring. The inner D ring contains D72 and D68 and is composed primarily of forward-scattering material, while the outer D ring is the zone around D73 which contains both forward-scattering and back-scattering components.

4. Photometric and spectroscopic properties of the high-phase D ring

The differences between the forward-scattering and back-scattering profiles of the D ring indicate that this region contains a mixture of particle populations. Detailed photometric and spectroscopic studies should provide constraints on the particle size distribution as a function of orbital radius, which in turn will yield information about any particle transport processes operating in this ring. Furthermore, accurate photometric measurements should resolve whether the material in Voyager's D72 has been lost from the ring, or simply spread over a wider range of orbital radii. However, such an analysis would be premature at this time because the absolute calibrations of the various Cassini instruments still need to be cross-checked against ground-based and HST measurements. In addition, we have not yet developed a robust algorithm for isolating the D-ring signal from the stray light produced by the planet and the main rings. We therefore must postpone a thorough analysis of the D-ring's light-scattering properties for a later paper. However, Cassini has obtained a few measurements which allow us to make some preliminary statements about the D-ring's forward-scattering components. These data were taken during times when the spacecraft passed through Saturn's shadow, enabling Cassini to observe the rings at very high phase angles (between 165° and 175°), or equivalently, very low scattering angles (scattering angle = 180° − phase angle).

4.1. ISS photometric data

During a high-phase opportunity on day 123 of 2005, the ISS instrument took a series of WAC images of the C and D rings over a period of about 30 min. At the start of this sequence, the Sun was located roughly 5° from the camera's boresight, moving out beyond 10° by the end of the observation. Furthermore, the WAC's field of view was sufficiently large that D-ring features were observed over a range of roughly 2°–3° in phase angle within each individual image. After navigating these images (in this case, for reasons that are still under investigation, the preliminary SPICE kernels provided a better fit to the observed ring features than the final kernels), we computed the apparent radius and phase angle of every point in six images taken with the CL1/CL2 filter combination, and then binned these data as a function of phase and orbital radius.

At these exceptionally high phase angles, the D ring is actually brighter than the inner C ring, so contaminating stray light is minimal. We can therefore use these data to produce densely sampled phase curves for phase angles between 170° and 175° (or, equivalently, between scattering angles of 10° and 5°). Fig. 5 shows the resulting phase curves for six features in the D ring, plotted as function of scattering angle θ. For four of these features, including the peak of D73, we simply plot the mean normal I/F as a function of scattering angle. For the D68 and D72 ringlets, we plot a quantity known as the equivalent width, defined as

$$\text{equivalent width} = \int \mu(I/F - I/F_{\text{bg}})\,\mathrm{d}r, \tag{1}$$

where μ is the cosine of the emission angle, I/F is the measured brightness as a function of radius and I/F_{bg} is the background level estimated from regions 300 km (D68) or 400 km (D72) wide on both sides of the ringlet. We plot the equivalent

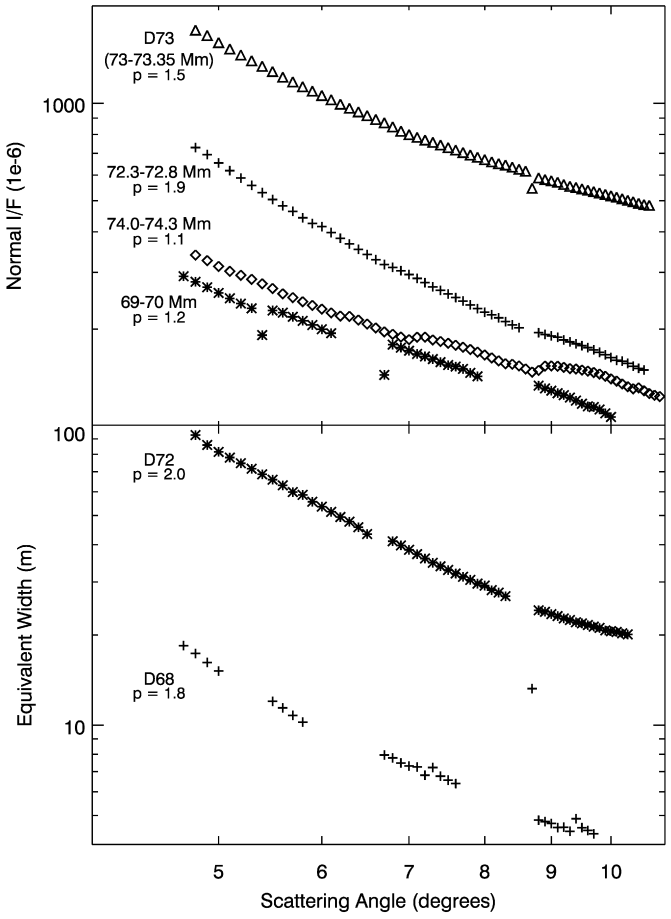

Fig. 5. Partial phase curves of various D-ring features derived from six ISS images (W1493791439, W1493791755, W1493792275, W1493792455, W1493793115, W1493793295; resolution 24 km/pixel, exposure duration 1.2 s) taken at exceptionally high phase angles (low scattering angles). The upper panel gives mean I/F versus scattering angle (180° − phase angle) over several D-ring regions, including the peak of D73. The bottom panel shows the equivalent width of the D68 and D72 ringlets, using the ranges 67,500–67,800 and 71,300–71,700 km as the regions of integration with the ranges 67,200–67,500, 67,800–68,100, 70,900–71,300 and 71,700–72,100 km defining the background level. The data are presented on a log–log plot to illustrate that each curve can be well fit with a simple power law (which is a straight line on this graph). The value of p associated with each curve is the power law index of a fit to the brightness as a function of scattering angle ($I/F \propto \theta^{-p}$). Note the "glitches" in the phase curves around 9° and 7°. These correspond to the edges of various images and are either due to minor errors in the pointing geometry or small amounts of stray light from Saturn's limb in the images.

width instead of the mean I/F for these ringlets because the former isolates the ringlet signal from the diffuse background and because it provides a more robust estimate of the amount of material in unresolved features such as D68.

All of the features plotted show steep rises in brightness with decreasing scattering angle, as we would expect for small, forward-scattering particles. Note that the slopes of these phase curves vary among the different ring regions, as was the case in the Voyager data (Showalter, 1996).

4.2. VIMS spectroscopic data

Another set of high-phase data was obtained on day 215 of 2005 when the VIMS instrument acquired four "image cubes" of the D ring, each one consisting of a 32 × 32 pixel array of brightness measurements at 352 discrete wavelengths between 0.35 and 5.1 microns. These cubes contained significant residual background signals after the standard calibration procedures, and owing to differences in how the data from the short-wavelength VIS channels and long-wavelength IR channels are measured (Brown et al., 2004), different subtraction procedures were necessary for the VIS and IR data. In particular, the VIS channel images showed strong vertical banding due to varying background in the CCD pixels, which is absent in the IR data. Fortunately, the bands were almost orthogonal to the D-ring features, so we could remove the banding by simply subtracting the mean signal from each column in the image at each wavelength. After this correction, we navigated the images and binned the data to produce an average spectrum for each orbital radius in each cube. The four cubes were taken over the course of about thirty minutes, during which time the Sun's apparent position relative to the instrument's boresight changed. However, for this analysis, we have simply averaged the data from the four cubes together to improve signal-to-noise in the spectra. The average phase angle for these observations was 167°, with a spread of ±2°. Finally, we removed a residual smoothly varying background spectrum from the combined profiles as follows: for each wavelength, we took the signal measured in the darkest parts of the image (the gap between 71,800 and 72,100 km, and the gap exterior to the feature around 74,100 km), fit an offset (in VIS channels) or an offset and a slope (in IR channels) to the brightness as a function of radius to these data, and extrapolated it to all other radii.

Fig. 6 shows the average spectra for four D-ring regions. The inner D ring lay mostly outside of the VIMS field of view at this time, so we do not have spectra of D68 or the diffuse material between D72 and D68. We do have spectra of both D72 and D73, as well as spectra of the strongly forward-scattering material interior to D73 and the structure around 74,100 km. All these spectra display a strong absorption band at 2.9 microns, diagnostic of water ice. D73 also shows a weaker water ice absorption band at 2.0 microns, and a similar feature may be observable in the 74,100-km complex, but the signal-to-noise is low. Outside of the 3-micron band, the various D-ring spectra show different spectral slopes, including a generally red slope between 1 and 3 microns. The lack of any methane signatures

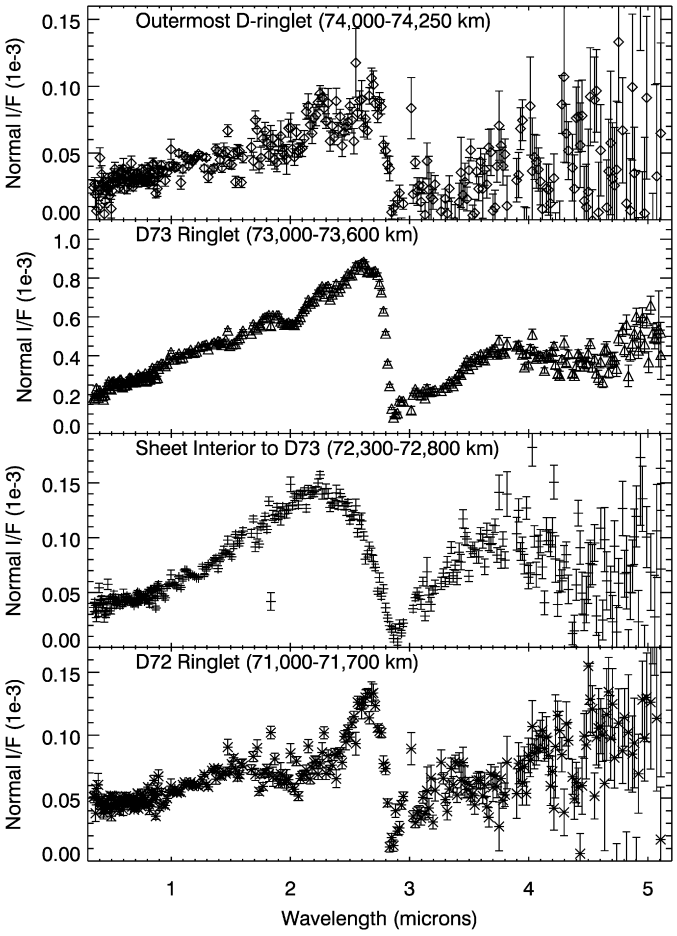

Fig. 6. Spectra of various D-ring regions derived from four VIMS cubes (V1501671495, V1501671856, V1501672216, V1501672576) taken at a phase angle of around 167° and a resolution of ∼50 km/pixel. All spectra show a characteristic absorption band at 3 microns due to water ice. Differences in this band's shape and the spectral slopes outside this band are sensitive to the typical particle sizes in these regions.

in the ring demonstrates that stray light from Saturn is not an issue for this data set.

4.3. Constraints on particle size distributions

Combining the above photometric and spectral data with theoretical models of light scattering by water-ice grains provides some preliminary information about the particle size distributions in these ringlets. Our model phase curves and spectra are computed with a Mie-scattering code that has been extended to include irregular particle models using the techniques outlined in Pollack and Cuzzi (1980) and Showalter et al. (1992). The current program assumes all particles are composed of pure water ice (optical constants provided by D. Cruikshank) and computes the integrated light scattered by any specified particle-size distribution. For this preliminary analysis, we have considered only simple end-member models: power-law distributions with cut-offs above 100 microns and narrow Hansen–Hovenier distributions:

$$n(r) \propto \left(\frac{r}{a}\right)^{1/b^2-3} e^{(1-r/a)/b^2}, \quad (2)$$

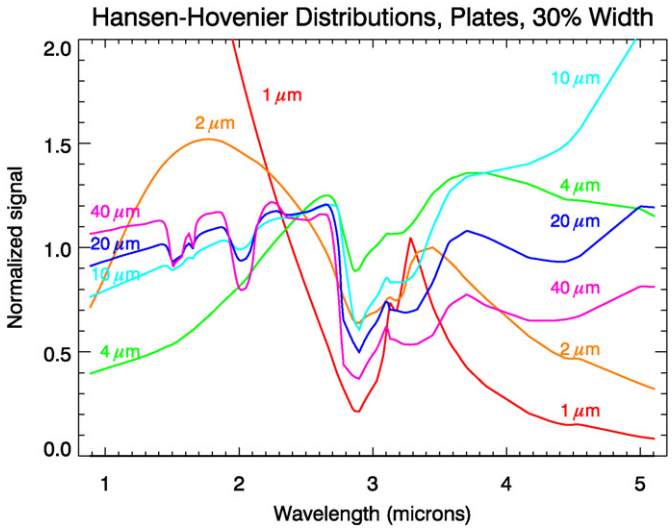

Fig. 7. Model infrared spectra of narrow Hansen–Hovenier distributions of water-ice grains at a phase angle of 166°. The labels on the curves denote the mean particle size of the distributions, all of which have a width of 30% in particle size and scattering properties based on the "plates" model (Number 5) of Pollack and Cuzzi (1980). Note the slope of the spectrum goes from red to blue with decreasing particle size, and that the shapes and depths of the ice bands change systematically with grain size.

where a is the mean particle size and b sets the distribution width.

Fig. 7 shows model spectra for various Hansen–Hovenier distributions with different mean particle sizes and widths equal to 30% of the mean particle size. The spectra are all computed for phase angles similar to those of the VIMS observations. Note that the depths of the ice bands increase with increasing mean particle size, with the 1.5- and 2-micron ice bands only visible for mean particle sizes greater than 10 microns. Also note that as the mean particle size increases from 4 to 40 microns, the slope in the 1–3-micron region becomes shallower, while for mean particle sizes smaller than 1 micron, the spectrum has a strong blue slope.

The observed spectra (Fig. 6) generally have a red spectral slope between 1 and 3 microns and a deep band at 3 microns. This indicates that the D ring does not contain large numbers of particles smaller than one micron, since such particles tend to exhibit a weak 3-micron band and a strong blue spectral slope. The weakness or absence of the 2-micron ice band indicates the forward-scattering component of these rings does not contain many particles much larger than 40 microns, because such large grains have sufficient path-length to produce obvious 2-micron bands. For these reasons, we find the size distributions of the forward-scattering components of the various D-ring features are better approximated by the narrow Hansen–Hovenier distributions than our power-law models with cut-offs above 100 microns. However, even the model Hansen–Hovenier spectra do not provide perfect fits to the observed trends. For example, a model spectrum with a typical particle size of 4 microns has a sufficiently red slope between 1 and 3 microns to reproduce that observed in D73, but it does not yield a sufficiently deep 2-micron ice band and does not reproduce the low signal levels observed beyond 3 microns. These discrepancies probably arise because the true particle size distribution differs from either of the simple cases we have considered thus far (for example, the distributions could be power laws with cut-offs in the 10-micron range). Furthermore, there may be non-water-ice contaminants in the D ring that could both change the slope between 1 and 3 microns, and reduce the 1.5- and 2-micron ice band strengths. A future publication will do a more comprehensive photometric analysis including a broader range of particle size distributions and compositions.

In spite of the limitations of our models, if we presume the variations in spectra are primarily due to changes in particle size distribution, we can at least note the following:

- The shallow red slope and the sharp short-wavelength edge of the 3-micron band in the spectrum of the 74,100-km complex are consistent with a distribution dominated by grains larger than 10–20 microns.
- The steeper red slope of D73 indicates this region contains somewhat smaller particles, but the presence of a detectable 2-micron ice feature indicates the typical particle size is roughly ∼10 microns.
- The material interior to D73 shows a softer short-wavelength edge of the 3-micron band and a broad peak around 2.5 microns, which is consistent with models having a mean particle size around 2 microns.
- The spectrum of D72 is least like the model spectra, with an unusual peak on the short-wavelength side of the 3-micron dip. Also, while there is no discernible 2-micron band, there appears to be a broad absorption between 1.7 and 2.5 microns. This may indicate the presence of a non-water-ice component in this ring, although we cannot yet rule out the possibility of a peculiar particle size distribution in this region or even some subtle error introduced by incomplete background subtraction.

We can also compare the phase data to model predictions. Over the limited range in scattering angle θ observed, all of the curves can be approximated by the simple power-law form

$$I/F \propto \theta^{-p} \tag{3}$$

with residual errors of order 5–10%. The best-fit values of p for the six regions considered here are provided in Fig. 5. The D68 and D72 ringlets—as well as the region just interior to D73—have the steepest phase curves, with $p \simeq 2$. D73 itself has an intermediate value of $p \simeq 1.5$. The diffuse material located between D72 and D68 and the ringlets around 74,100 km have the shallowest phase curves, with $p \sim 1.2$.

Fig. 8 shows the power-law index p between scattering angles of 4° and 12°, calculated from our unimodal models, as a function of mean grain size. This graph indicates that p grows with increasing particle size until reaching a maximum around 2–3 microns, at which point p declines again. Thus p does not favor a unique mean particle size. However, we can use the spectral data to decide on which branch of this curve the D ring's various components probably lie.

Please cite this article in press as: M.M. Hedman et al., Saturn's dynamic D ring, Icarus (2007), doi:10.1016/j.icarus.2006.11.017

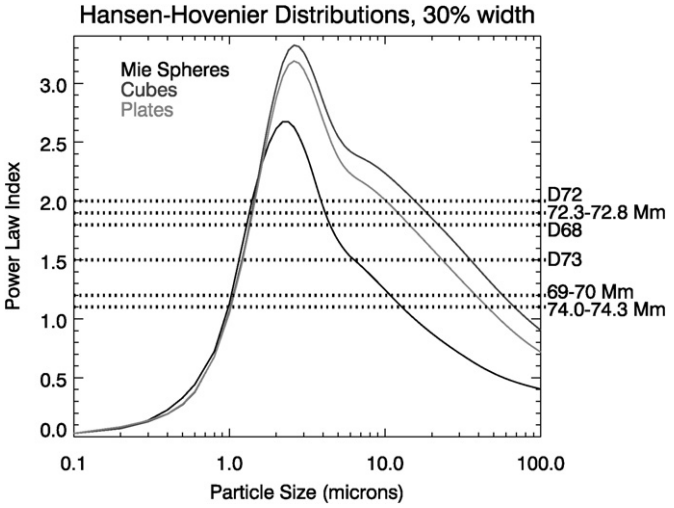

Fig. 8. The value of the power-law index p between scattering angles of 4° and 12° as a function of mean particle size for unimodal, 30%-wide Hansen–Hovenier distributions of ice grains, assuming a wavelength of 600 nm. The three curves correspond to ideal Mie spheres and two semi-empirical models (3 "Cubes" and 5 "Plates") from Pollack and Cuzzi (1980). Horizontal dotted lines show the measured values of the power-law index from Fig. 5.

For the D68 and D72 ringlets and the material interior to D73, $p \simeq 2$, near the peak in the curve, consistent with the typical particle size in all of these regions being between 1 and 10 microns, which agrees with the spectral data. The spectral data indicate that the outer parts of the D ring contain larger particles than the inner regions, so we expect the regions between D73 and the C ring fall on the high-particle-size branch of the curve. D73, with a $p \simeq 1.5$, then appears to be dominated by particles 5–30 microns across, and the 74,100-km complex ($p \simeq 1.1$) has particles roughly 40 microns across. By contrast, we expect the diffuse material between D68 and D72 would be composed of smaller particles than D72 itself, so we assume here the distributions fall on the low-particle-size branch. In this case $p \simeq 1.2$ would indicate that particles roughly 1 micron across dominate in the region between D68 and D72.

This analysis therefore suggests that grain size generally increases with orbital radius, with the smallest (∼1 micron) particles occurring in the diffuse material in the inner D ring; somewhat larger (1–10 microns) particles in D68, D72 and the inner part of the outer D ring, and still larger (10–100 microns) grains within and exterior to D73. Given the limitations of our model, we caution against over-interpreting these results, since there could well be other explanations for the observed trends beyond changes in the "mean particle size." For example, the spectral changes could reflect more complex shifts in the distribution function, such as variations in the ratio of 40-micron-sized particles to 2-micron-sized particles. There also could be variations in the distribution of various contaminants in the ring. However, this preliminary analysis of the D-ring's photometric and spectroscopic properties does suggest that all parts of this ring contain ice grains between 1 and 100 microns across, and that there are significant changes in particle properties with orbital radius. No other known dusty ring has such radical fine-scale variations in particle size with location (cf. Showalter, 1996; Burns et al., 2001), and it suggests that the dominant perturbations on grains vary strongly with both particle size and orbital radius. Almost all non-gravitational evolution mechanisms (cf. Burns et al., 2001) have this character. We also remind the reader that this analysis only considers the strongly forward-scattering component of the D ring, and a radially-variable population of larger, more back-scattering particles likely occupies this region as well.

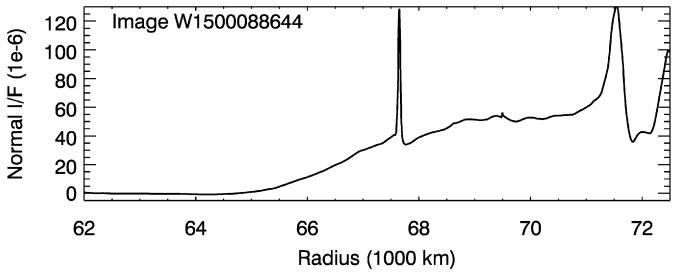

Fig. 9. A closer look at the diffuse material in the inner D ring. This profile is derived from the same high-phase (171°) observation of the D ring used in Figs. 2 and 4 (17 km/pixel resolution, 3.2 s exposure duration) with a constant background removed. The D ring starts at around 65,000 km and, moving outwards, steadily increases until D68 is reached. Since the I/F drops slightly outside D68, D68 itself may be the source of much of the diffuse material in the ramp between 65,000 and 68,000 km. Subtle variations in I/F are visible between D68 and D72. The cusps around 68,500 and 69,500 km are due to image-compression artifacts.

5. Detailed survey of D-ring morphology

With the above overview of the D-ring's gross structure and composition, we can now turn to the detailed morphology of the various D-ring features, beginning at the inner edge and working outwards. Special attention will be paid to those features that seem to be variable in time and/or longitude.

5.1. The inner D ring

5.1.1. Diffuse material

The photometric properties of the diffuse material interior to D72 are consistent with a population of small particles. These grains may have been derived from D72 and then spiraled inward towards the planet under the influence of Poynting–Robertson and other drag forces (Burns et al., 2001). Fig. 9, the highest signal-to-noise profile of this material obtained in the first two years of the Cassini mission, shows that the I/F between D68 and D72 is higher than it is exterior to D72. Between 69,000 and 71,000 km the I/F is relatively constant with only subtle, quasi-periodic variations with a typical length scale of ∼500 km. The wavelength of this structure is comparable to that seen by Voyager in this region (Marley and Porco, 1993; Showalter, 1996), but the amplitude of the fluctuations is an order of magnitude smaller. Interior to 69,000 km, the brightness of the material declines, only to increase sharply just interior to D68. The brightness then continues to decay until the signal disappears around 65,000 km (cf. Fig. 1; Showalter, 1996).

The pronounced drops in the brightness of this diffuse material exterior to the D72 and D68 ringlets suggest that D72 and

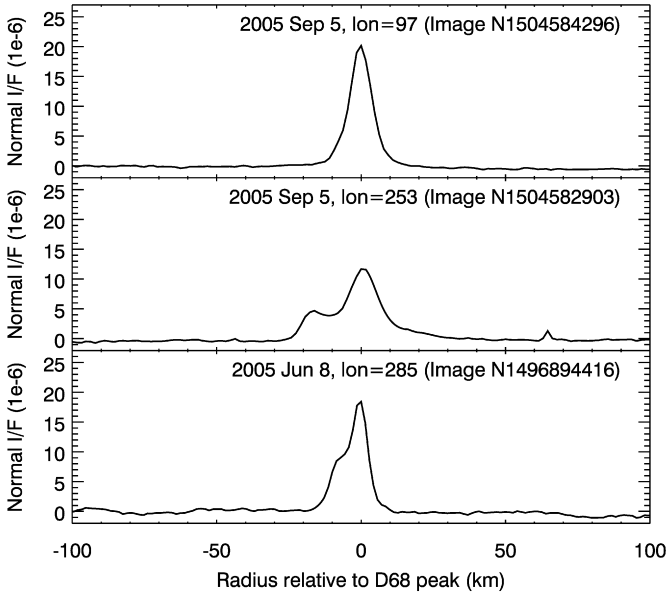

Fig. 10. High-resolution profiles of D68 obtained at low phase angles (between 10° and 20°). The top two profiles were taken of opposite ansae at nearly the same time and with the same resolution (roughly 3 km/pixel) and exposure duration (3.8 s), while the bottom profile was obtained three months earlier at a slightly better resolution (2 km/pixel) and shorter exposure duration (1 s).

D68 are sources for the material in the sheets. If the ringlets act as sources of material, then the material interior to D68 may be derived from both D68 and D72, while the material between D72 and D68 should come primarily from D72. Detailed photometric studies of these regions are underway to see if compositional or particle-size differences can be detected between these two diffuse components.

5.1.2. D68

The D68 ringlet has been observed at phase angles ranging from 10° to 175°. While it is brightest at high phase angles, the best-resolution images of this feature were obtained at low phase angles. Fig. 10 plots our three highest-resolution profiles of this feature (2–3 km/pixel). One profile exhibits a simple Gaussian shape with a FWHM of approximately 10 km, whereas a second profile—obtained at nearly the same time as the first but at a different longitude—displays two distinct components, separated by 15 km. The third profile, taken two months earlier, contains two components separated by only 5 km. If all of these features lie in the same plane, then the detailed radial structure of D68 varies with longitude and time (alternatively, the second component of D68 may be inclined out of the equatorial plane).

All other D-ring images from Cassini lack the required resolution to discern the second component of D68. However, these additional images reveal that D68's radial location varies in time and/or longitude. When the profiles are shifted so that the inner C ring, D73 and D72 are aligned (generally to within 15 km), the position of D68 ranges over ±40 km (see Table 1). Such shifts could be interpreted as evidence that D68 is eccentric and/or inclined. However, a closer look at the data reveals that the situation is probably more complicated.

The Cassini data include two high-resolution, nearly simultaneous observations of both ansae of D68. If D68 was a simple eccentric ringlet with zero inclination, then the average of two radii measurements ∼180° in longitude apart would always yield the same value, the ring's semi-major axis. However, in one sequence (N1504582903/N1504584296) the opposite ansae of D68 were at apparent radii of 67612.5 ± 0.2 km and 67647.2 ± 0.2 km, while in the other sequence (N1493557225/N1493559711) they were at apparent radii of 67650.0 ± 1.6 km and 67697.0 ± 1.5 km. The average values for these two pairs (67639.9 and 67673.5 km, respectively) are significantly different, which is inconsistent with an equatorial, eccentric ringlet. If we instead attempt to fit these data to an inclined, eccentric ringlet (allowing the longitudes of the apses and nodes for the two observations to float because of the large uncertainties in the precession rates this close to Saturn) then the relatively large ring opening angle $B \sim 15°$ for all the observations requires an inclination $\sin I > 0.001$ and a comparably large eccentricity. However, if D68 had such a large inclination and eccentricity, then we would expect the position of D68 among the remaining observations to scatter over ±60 km. Instead, a majority of the observations—including some with $B \sim 5°$—find D68 within 10 km of 67645 km (see Table 1). We therefore suspect that D68 cannot be modeled by an inclined eccentric ringlet, but instead has a more complex shape, perhaps including higher-order modes analogous to those found in some of uranian rings (French et al., 1991). Testing this hypothesis is difficult at present owing to the large precession rates of such patterns and the sparseness of the available observations. Future Cassini observations—including high-resolution movies of D68—should allow us to clarify the dynamics of this ringlet.

5.1.3. D72

Compared to the ∼40-km wide ringlet observed by the Voyagers (Showalter, 1996; Fig. 1), today's D72 is much more diffuse, with a FWHM of ∼300 km around a center of light at 71,500 km. Like D68, this feature has been observed at phase angles from 10° to 175°, and is brightest at the largest phase angles.

At present, two low-phase images of D72 have sufficient resolution and signal-to-noise to detect brightness variations within the ringlet (see Fig. 11). Structure within D72 can also be detected in a series of observations at high phase angles with 2–3 times lower resolution (see Fig. 12). Both of the low-phase observations show quasi-periodic brightness variations with wavelengths between 40 and 60 km, and a similar pattern may be barely resolved in the high-phase profiles. The low-phase data show that the wavelength of this structure is variable with time and/or longitude. Two possible explanations for such variations are (1) that the pattern is due to satellite wakes similar to those produced by Pan and Daphnis in the A ring (Showalter et al., 1986; Porco et al., 2005) and (2) that the pattern is a winding spiral. Unfortunately, neither of these models provides a completely convincing match to the data.

A tiny moonlet orbiting in the "gap" between the inner and outer D ring, just exterior to D72, could produce quasi-periodic brightness variations with a wavelength that depends on the ob-

Table 1
Measured positions of the D68 ringlet

Image	Image mid-time	Phase angle	Emission angle	Longitude[a]	Radius
N1504582903	2005-248T03:13:26	12.1	105.8	253.3	67612.5±0.2[b]
N1504584296	2005-248T03:36:39	10.6	105.7	97.3	67647.2±0.2[b]
N1496894416	2005-159T03:26:56	19.6	106.4	284.6	67645.4±0.2[b]
N1493557225	2005-120T12:33:19	33.3	109.5	55.5	67650.0±1.6[b]
N1493559711	2005-120T13:14:45	38.4	109.5	219	67697.0±1.5[b]
N1466448054[c]	2004-173T04:00:00[c]	66.9	106.1	175	67636[d]
N1485865825	2005-031T12:04:09	76.0	94.4	180	67628[d]
N1485708324	2005-029T16:19:09	78.9	94.3	180	67646[d]
N1485518423	2005-027T11:34:10	82.7	94.4	177.5	67666[d]
W1477670473	2004-302T15:36:24	144.1	84.1	222.5	67594[d]
W1501674109	2005-214T11:13:52	165.6	110.9	265	67640[d]
W1493793295	2005-123T06:07:16	171	71.2	248.5	67640[d]
W1500088644	2005-196T02:49:36	171	67.2	280	67647[d]

[a] Inertial longitude in Saturn's equatorial plane, defined relative to the intersection of that plane and Earth's equatorial plane in J2000 coordinates.
[b] Formal error bars from a Gaussian fit to D68. There is also an additional systematic pointing uncertainty for each image. In the first three high-resolution images this uncertainty is around 1 km, while in the last two, somewhat lower-resolution images, it is around 5 km. (In both cases, the systematic error is approximately 0.5 pixels.)
[c] These data come from a sequence of 118 images beginning with the named image, the time given here is the mean time of the entire sequence.
[d] The formal error bars on these measurements are on the order of 5 km. However, in these lower-resolution scans, the systematic pointing uncertainty dominates (approximately 15 km for all of these observations).

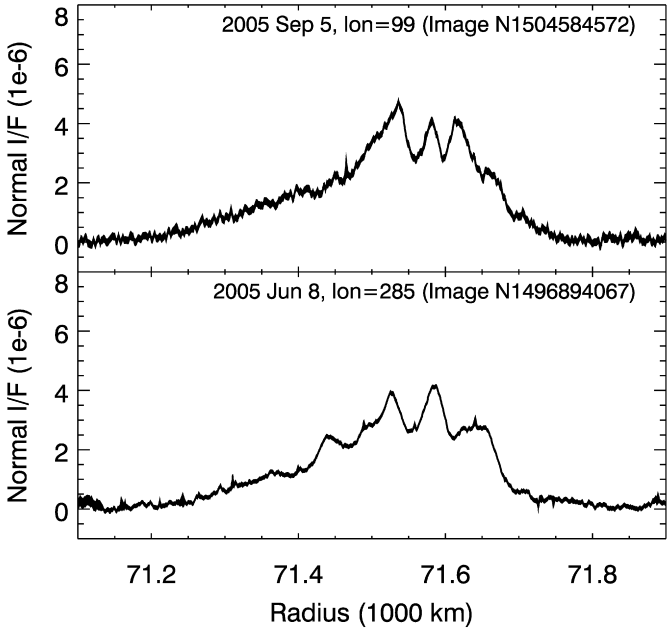

Fig. 11. High-resolution (2–3 km/pixel) profiles of D72 obtained at low phase angles (10°–20°). The line thickness shows the 1-sigma uncertainties per pixel-width radial bin due to random variations (exposure durations are 3.8 and 10 s, respectively). Both profiles both show quasi-periodic oscillations in I/F atop the ringlet. The wavelength of this variation is about 40 km in the top profile and around 60 km in the bottom profile.

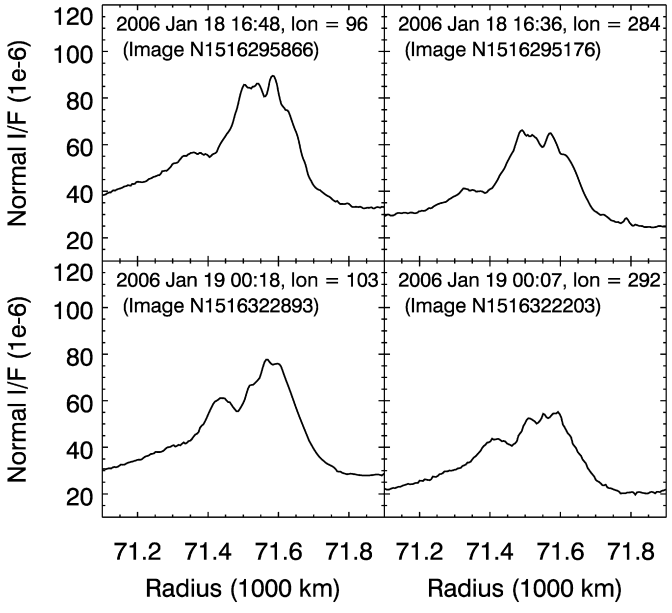

Fig. 12. Profiles of D72 obtained at phase angles between 150° and 160° with a resolution of 7 km/pixel and exposure duration of 1 s. This sequence imaged both ansae of the D ring over an extended period of time. The top pair of profiles was obtained from observations taken 8 h before those that produced the bottom pair of profiles.

served region's longitude relative to the Moon. The standard expression for the radial wavelength of such a wake is (Showalter et al., 1986)

$$\lambda = \frac{3\pi(a_s - a)^2}{a_s \theta}, \tag{4}$$

where a is the semi-major axis of the wake, a_s is the semi-major axis of the perturbing Moon, and θ is the longitude difference between the observed wake and the Moon (in radians). We can obtain a value of λ consistent with the observed values if we assume $a_s \simeq 71{,}900$ km and $\theta \simeq 20°$ for both observations. However, the high-phase data suggest that a ∼40-km wavelength pattern was present at both ansa at the same time (see Fig. 12), which is inconsistent with this model.

Alternatively, the structure could be attributed to a spiral pattern like those found in the F ring (Charnoz et al., 2005) and in the outer D ring (see below). Such a pattern will have the same radial wavelength at both ansa at the same time, but the wavelength should decline over time due to orbital shear. While the wavelength does decline from ∼60 to ∼40 km during the three months between the two low-phase observations, the pattern's wavelength in the high-phase observations—taken three months after the last high-resolution, low-phase observation—also lies between 40 and 60 km. We therefore do not observe a clear monotonic decrease in wavelength over 6 months, indicating that the pattern is not a simple spiral pattern. (We also do not detect contrast reversals across the ansa in these observations, so this structure probably cannot be attributed to a vertical corrugation like that described below in the outer D ring.)

The high-phase observations of D72 also display a secondary hump on D72's inner flank, around 71,400 km. Strangely, this bump is rather diffuse and centered at 71,350 km in two images of different longitudes in the D ring taken at approximately the same time (N1516295176, N1516295866), but becomes sharper and peaks between 71,400 and 71,450 km at both ansae in images taken 8 h later (N1516322203, N1516322893). If this represents a true radial movement of material, particles would have to be moving outward between 10 and 20 km/h. We are not aware of any mechanism that could transport material radially at this speed. Alternatively, the radial location of this density enhancement could be longitudinally variable with a large $m = 2$ component. In this case, the density enhancement would appear to move in and out simultaneously at both ansa. Such an azimuthal structure may also be related to the apparent changes in the pattern atop D72 itself. Additional high-resolution observations on this region are planned that should help clarify how the substructure in D72 changes with longitude and time.

5.2. *The outer D ring*

5.2.1. *Diffuse material interior to D73*

Images taken at high phase angles detect a shelf of material extending interior from D73 to about 72,500 km (see Fig. 4). As discussed in Section 4, this material is strongly forward-scattering, and it is almost invisible at phase angles below 140°. This region therefore appears to contain more particles in the 5–10-micron size range than other parts of the outer D ring. Perhaps this feature consists of material spiraling inwards from D73, just as the diffuse material in the inner D ring may derive from D68 and D72.

5.2.2. *D73 and the trans-D73 region*

The region between D73 and the C ring is by far the most complex part of the D ring. High-resolution images of this region (see Figs. 13 and 14) show that it contains significant structure on scales around 30 km and less.

Fig. 15 compares two profiles of the outer D ring, one taken from a high-phase, 7 km/pixel observation (Fig. 14) and one from a higher-resolution (1.6 km/pixel), low-phase observation (Fig. 13). As discussed below, these profiles contain considerable fine-scale structure. First, however, we must call attention to the medium-scale features that appear as peaks in the high-phase profiles, but as dips in the low-phase profiles.

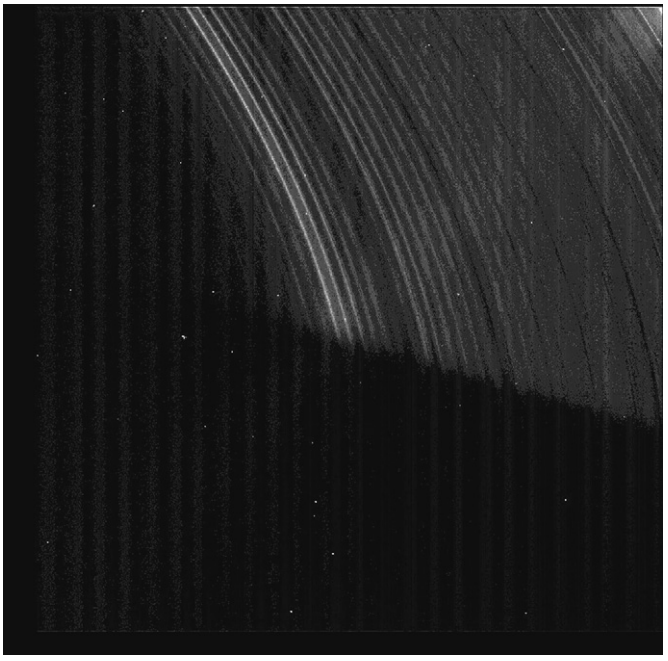

Fig. 13. One of the highest-resolution image of the outer D ring (72,500–74,500 km) taken to date by the Narrow-Angle Camera on Cassini (N1495333419, at a phase angle of 41°, with a resolution of 1.6 km/pixel and an exposure duration of 0.46 s). This image has been rotated clockwise 90° so that the rings have a similar orientation as those elsewhere. The over-exposed inner edge of the C ring lies at the upper right-hand corner of this image, while the planet's shadow cuts across the lower part of the image. D73 corresponds to the innermost 2–3 bright features. The vertical banding is an instrumental artifact that forms horizontal bands in the original unrotated image (Porco et al., 2004); it has been partially subtracted from this image for display purposes. A radial profile derived from this image is shown in Fig. 15.

Exterior to D73, peaks in the high-phase profiles occur at radii of 73,450, 73,700, 74,070 and 74,180 km. Smaller peaks can be identified at 74,280, 74,350 and 74,420 km. Each high-phase peak corresponds to a low-phase dip, with the peaks somewhat exterior (by about 20 km) to the corresponding dips. For the innermost two peaks, these dips correspond to regions where the strength of the fine-scale 30-km structure is reduced. This pattern is also apparent in lower-resolution images at intermediate phase angles (∼80°, not shown), where a slight rise can be seen exterior to the dips at 73,450 and 73,700 km. Some process must be affecting the particle size distribution in these regions, generating an excess of small forward-scattering particles and a deficit of larger, back-scattering particles. These features occur at essentially the same radii in all images taken at comparable phase angles, making them useful fiducial points for studying the finer-scale structure, which is much more variable.

The low-phase profile in Fig. 15 clearly reveals two very different types of fine-scale structure. Between 73,200 and 74,000 km, the fine-scale variations are remarkably regular, with a wavelength of ∼30 km, which will be discussed at length in Section 6 below. Exterior to 74,000 km, the fluctuations are

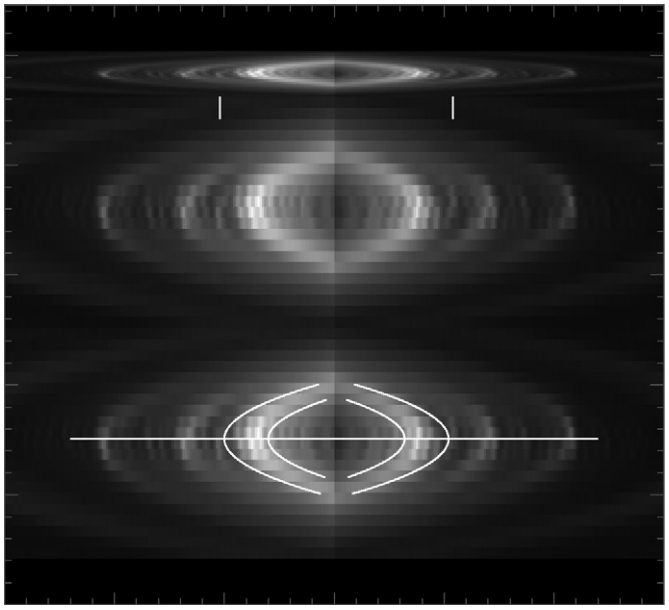

Fig. 14. High-resolution images of the outer D ring at high phase angles (N1516295176 and N1516295866). Resolutions are approximately 7 km/pixel, exposure durations are 1 s, and the phase angles are between 150° and 160°. These two images of the ansae were taken nearly simultaneously. The images have been cropped for presentation. The top panel shows the original data, while the images in the lower two panels have been vertically stretched by a factor of 5 to make the vertical structure clearer. The bright region that lies between the pairs of arcs in the bottom panel corresponds to the peak of D73. The vertically stretched images also show evidence for contrast reversals across the ansa. To guide the eye, the bottom panel includes a line that bisects the ansa and several arcs that illustrate how circular ringlets should appear in this image. Note how the bright and dark bands above and below the line are 180° out of phase with each other. Profiles derived from these images are found in Figs. 15 and 18.

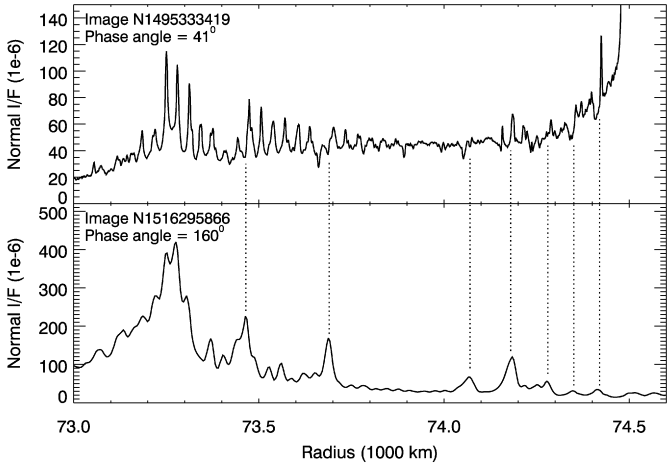

Fig. 15. Comparison of the morphology of the outer D ring at low phase (top) and high phase (bottom) derived from Figs. 13 and 14. The high-phase data have 3–4 times poorer resolution than the low-phase data (7 versus 1.6 km/pixel). The locations of peaks in the high-phase profile exterior to 73,400 (such as those at 73,450, 73,700 and 74,050 km) are marked with vertical lines and correspond to dips in the overall brightness of the low-phase profile with a slight radial offset of order 20 km.

much more chaotic, with no obvious wavelength. Many of the chaotic variations in the outermost D ring are probably below the resolution of the high-phase images, however the 30-km structure is visible, if muted, in the high-phase profile (Fig. 15).

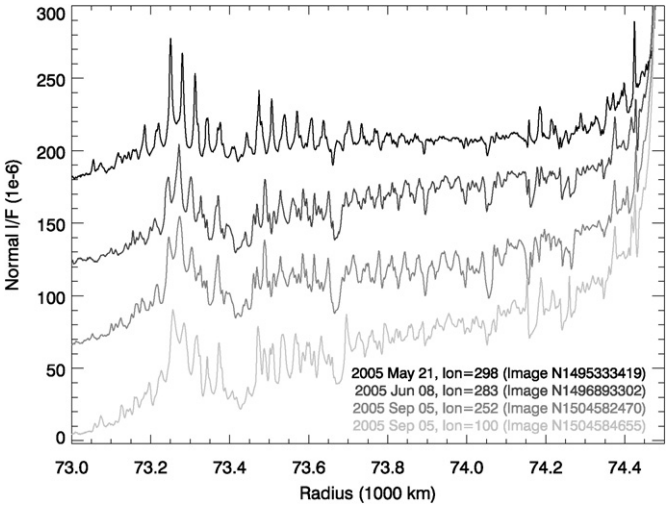

Fig. 16. A comparison of the four highest-resolution complete profiles of the outer D ring (the top curve is also shown in Fig. 15), with curves offset for clarity. These profiles were obtained at phase angles of 41°, 19°, 11° and 12°, with resolutions of 1.6, 2.2, 3 and 3 km/pixel and exposure durations of 0.46, 0.82, 0.68 and 0.68 s, respectively, from top to bottom. The bottom two profiles were measured on opposite ansae but at nearly the same time. Note the similarities and differences in the fine-scale structure among all these profiles.

Fig. 16 presents four profiles from our highest-resolution observations of this region. Exterior to 74,000 km, much of the fine-scale structure is different from profile to profile. Only a few bright features are identifiable in multiple curves, such as the narrow ringlets at 74,190, 74,350 and 74,420 km.

6. The periodic structure between 73,200 and 74,000 km

The periodic brightness variations between 73,200 and 74,000 km are among the D ring's most intriguing features. As discussed in detail below, observations of these brightness variations at low opening angles can be interpreted as evidence for periodic vertical corrugations in the outer D ring. Comparisons with earlier observations from HST provide evidence that this vertical corrugation is a winding spiral pattern produced by differential nodal regression. Finally, by extrapolating the available observations backwards in time, we infer that some event, possibly a meteoroid impact, altered the angular momentum of the outer D ring in early 1984.

6.1. Cassini observations: Evidence for vertical corrugations

A periodic brightness variation in this region is observed in the nine highest resolution observations of the outer D ring at low phase (see Fig. 16 for examples). Note that the brightness peaks do not in general align between different scans. In each scan, the period of this structure is nearly constant with radius, and indeed the variations in all nine scans can be fit well with a single sine wave having a variable amplitude and a wavelength between 31 and 34 km (see Fig. 17).

A 30-km fluctuation can also be observed in all of the highest-resolution, high-phase profiles (an example is shown in Fig. 15). The low opening angles of the rings during these observations also provide an important clue about the true nature

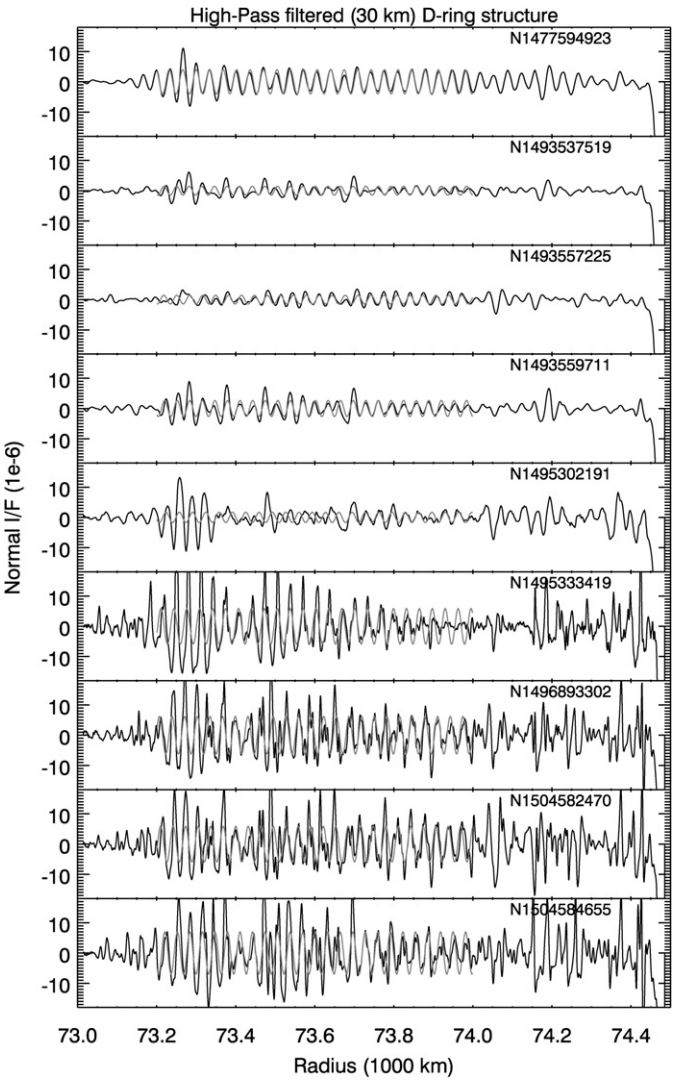

Fig. 17. A closer look at the ∼30-km periodic structure in the outer D ring, showing the nine highest-resolution, low-phase complete profiles obtained so far, after they were high-pass filtered to emphasize the fine-scale structure. The bottom four profiles are also shown in Fig. 16. All are taken at phase angles below 45°, and all show the ∼30-km structure. The light green (gray) curves are simple sinusoids, illustrating that—for any particular image—the wavelength of this structure is nearly constant with radius. Comparisons among these profiles demonstrate that not only does the phase of the ∼30-km structure change with longitude and/or time, but also that the structures' wavelengths vary between 31 and 34 km among the profiles. (Image statistics from top to bottom: phase angles = 33.3°, 40.7°, 33.3°, 38.4°, 1.1°, 41.2°, 18.1°, 13.2°, 11.8°; longitudes: 245°, 218°, 56°, 219°, 268°, 283°, 298°, 252°, 100°; resolutions (km/pixel): 7, 9, 9, 9, 3, 2, 2, 3, 3; exposure durations (s): 0.22, 2.00, 1.50, 2.00, 5.60, 0.46, 0.82, 0.68, 0.68.)

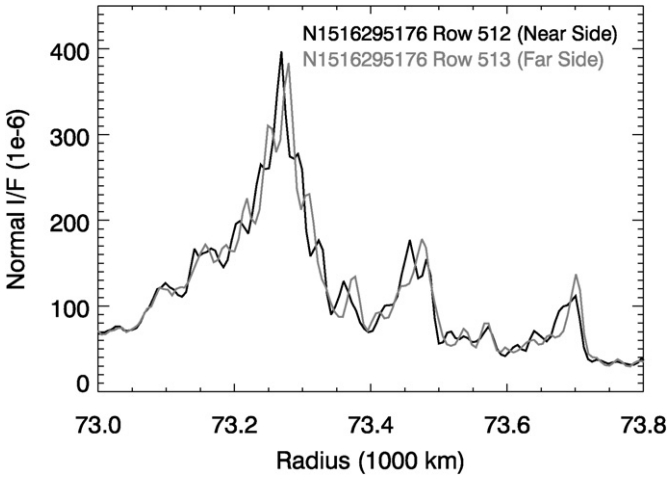

Fig. 18. Brightness profiles of the outer D ring derived from a single high-phase, low inclination image displayed in Fig. 14. The two profiles correspond to two different rows in the image, covering the near and far sides of the ansa, respectively. The navigation accuracy was confirmed by comparing the profiles in the C ring (not shown). Note that the overall brightness envelope, including the peaks at 73,450 km and 73,700 km are aligned in the two images, but that the 30-km periodic pattern is exactly 180° out of phase throughout this region. This near-perfect antiphase relationship is most easily explained in terms of contrast reversals due to a vertical corrugation.

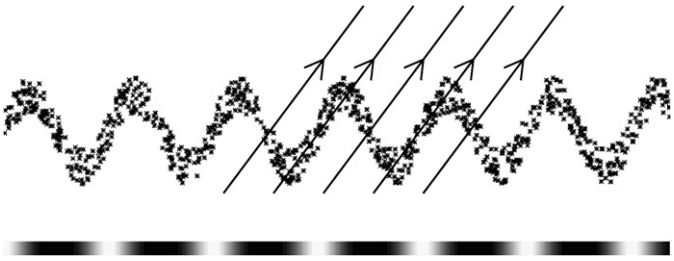

Fig. 19. A vertical corrugation in a diaphanous ring can give rise to brightness variations. The diagonal lines correspond to lines of sight through the corrugated ring. The gray-scale at the bottom shows the ring's total optical depth and brightness as seen by the observer.

of this periodic structure. Fig. 14 contains images of opposite ansae of the outer D ring taken at high phase at about the same time. In these images the ∼30-km pattern at first appears to consist of a series of narrow ringlets. However, these "ringlets" do not line up as one might expect if the material were all situated in Saturn's equatorial plane.

The lower two panels of Fig. 14 show vertically stretched versions of the images, and the bottom panel includes a horizontal line that bisects the ansae, as well as arcs indicating approximately lines of constant radius. These images reveal that each of the brightness peaks just below the ansa corresponds to a brightness dip just above the ansa and vice versa. Fig. 18 demonstrates that this pattern of "contrast reversals" is not an artifact of a small pointing error in the images. This figure shows two brightness profiles derived from two pixel rows in one of these images just above and just below the ansa. Both these profiles include part of the innermost C ring (not shown), where features in the two scans are aligned to within about 5 km. This confirms the accuracy of our image navigation, and gives us confidence that the almost perfect anticorrelation between the fine-scale brightness variations in Fig. 14 is a real feature of the rings.

We interpret this pattern of contrast reversals as evidence for a vertical corrugation in the ring material, based on a similar model that has been used to explain a better-resolved pattern of bright and dark patches observed in Jupiter's main ring (Ockert-Bell et al., 1999; Showalter et al., 2001). Fig. 19 illustrates how changes in the local slope of a warped ring lead to differences in the amount of material along different lines of sight (Gresh et al., 1986). These differences in optical depth trans-

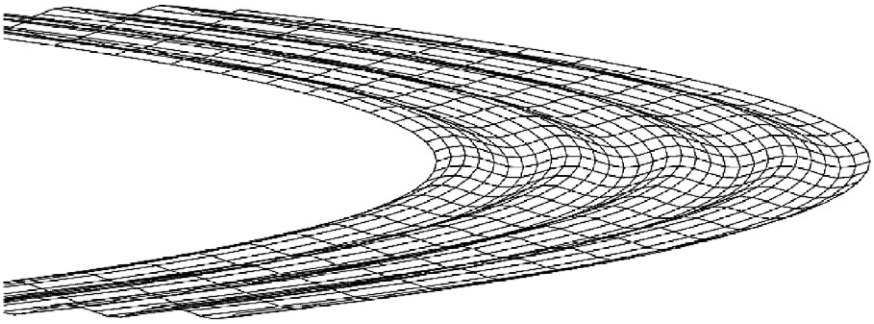

Fig. 20. A sketch illustrating how a vertical corrugation in the ringplane can lead to contrast reversals. This wireframe diagram displays a flat ring onto which is superimposed a vertical, sinusoidal pattern. The view is shown from nearly edge-on. Where the spacing of the lines of the diagram are closer, one would expect a ring to appear more optically thick along the line of sight, and so a faint ring would appear brighter. Furthermore, note that all features show a brightness transition as they cross the ansa: brighter features become darker and darker features become brighter.

late directly into variations in the observed brightness provided the optical depth of the material is sufficiently low, so the ring appears brightest when the ring surface is most parallel to the observer's line of sight. This occurs at different locations in the ring depending on the geometry of the observation, so vertical corrugations naturally lead to phenomena like contrast reversals at the ring ansa. As shown in Fig. 20, a ring region whose surface normal is canted towards the viewer's line of sight (and therefore appears fainter) on the far side of the ansa will have its surface normal tilted away from the line of sight (and therefore appear brighter) on the near side of the ansa.

Given that the contrast reversal is not very well resolved in the available D-ring data, there are possible alternative explanations for this pattern. For example, if the 30-km brightness variations in this region were due to a series of discrete ringlets with non-zero eccentricities or inclinations, then the apparent locations of these ringlets do not have to be symmetric about the expected ansa-line, and there are cases when such asymmetries could even produce patterns reminiscent of contrast reversals. In practice, however, it is very difficult to fit the observed data to series of continuous ringlets because the relative phase shift between the 30-km structure on the two sides of the ansa is so close to 180° (see Fig. 18). Furthermore, we need a relatively rare arrangement of ringlet nodes/pericenters and viewing geometry to produce a pattern of contrast reversals, whereas a vertically corrugated sheet will always produce contrast reversals in a faint ring if the ring opening angle is sufficiently low. We therefore regard the vertical corrugation model as the most parsimonious explanation of the present data.

Assuming that the D ring is vertically corrugated, we can estimate the amplitude of the correlation from the magnitude of the brightness variations. For a sufficiently thin ring, the line-of-sight optical depth of a given point on the ring is given by

$$\tau = \tau_o / |\hat{\mathbf{n}} \cdot \hat{\mathbf{o}}|, \tag{5}$$

where τ_o is the optical of the ring viewed at normal incidence, $\hat{\mathbf{n}}$ is the unit normal vector to the surface and $\hat{\mathbf{o}}$ is the unit vector pointing from the surface to the observer. Say the ring has uniform optical depth and the ring's vertical position z varies sinusoidally as a function of radius r with amplitude A and radial wavenumber $k = 2\pi/\lambda$ (i.e., $z = A\cos(kr)$). Furthermore, say the ring opening angle to the observer is B and ϕ is the angle between the observer's line of sight and the radial direction. Then we find τ as a function of radius is

$$\tau = \frac{(\tau_o / \sin B)\sqrt{1 + [Ak\sin(kr)]^2}}{1 + \cot(B_{\rm eff})[Ak\sin(kr)]}, \tag{6}$$

where $B_{\rm eff} = \tan^{-1}(\tan B / \cos\phi)$ is the "effective" ring opening angle of the observation (Gresh et al., 1986).

From this expression, we can compute the ratio of the maximum and minimum optical depths:

$$\frac{\tau_{\rm max}}{\tau_{\rm min}} = \frac{\tan(B_{\rm eff}) + Ak}{\tan(B_{\rm eff}) - Ak}, \tag{7}$$

and then obtain an expression for the corrugation amplitude A:

$$A = \frac{\lambda}{2\pi}\tan(B_{\rm eff})\frac{\tau_{\rm max} - \tau_{\rm min}}{\tau_{\rm max} + \tau_{\rm min}}. \tag{8}$$

Since the optical depth of the D ring is so low, the measured I/F is proportional to the optical depth τ, so we can use the ratio of brightnesses between the peaks and the troughs of the 30-km structure to estimate the amplitude A of the corrugation. Fig. 21 plots the values derived for one of our highest-resolution observations of this structure, which shows the corrugation amplitude peaks at about 1.5 km around 73,300 km and gradually declines outwards to zero around 74,000 km. The inclination of ring particle orbits in this region is therefore of order 10^{-5}.

6.2. *Temporal variations in the regular structure: Evidence for a winding spiral*

The most remarkable thing about this periodic structure is that it is not a static feature of Saturn's rings, but has instead undergone significant evolution over the last decade. On November 21–22, 1995, an occultation by the rings of the star GSC5249-01240 ($M_B = 12.2$) was observed using the Faint Object Spectrograph onboard the Hubble Space Telescope (Bosh and Olkin, 1996; Bosh et al., 2002; Bosh, in preparation). The ring-opening angle to Earth at this time was only 2.7°, making this occultation particularly sensitive to low optical-depth regions like the D ring. As the star passed behind the region between 73,200 and 74,000 km, a series of regularly spaced spikes with normal optical depths of roughly 0.002 were detected (see

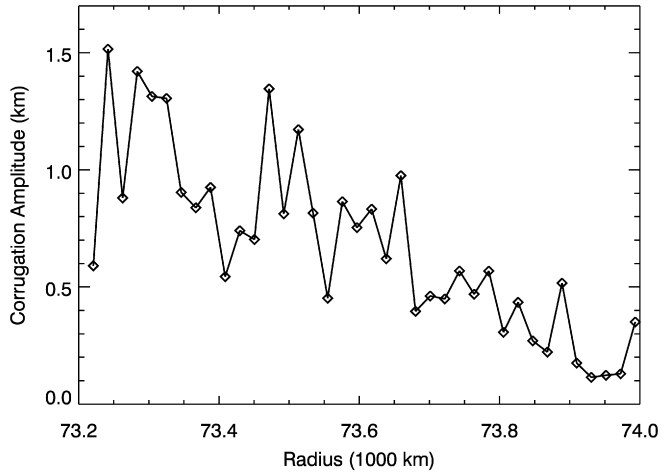

Fig. 21. Estimates of the vertical corrugation amplitude based on our highest resolution image of the D ring (N149533419, resolution 1.6 km/pixel, $B = 9.3°$, $\phi = 70°$, Fig. 15). Each amplitude estimate is derived using the ratio of a brightness peak to nearby brightness minima (both with a background level derived from the mean I/F between 72,600 and 72,700 km subtracted) using Eq. (8) and assuming $\lambda = 32.5$ km (see Table 2).

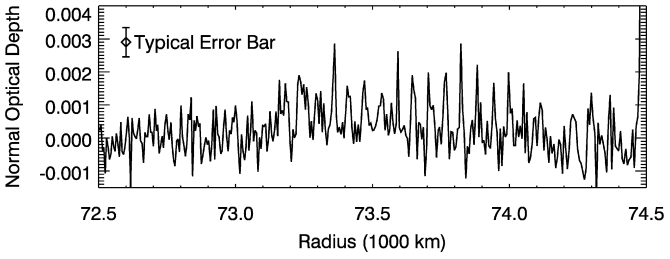

Fig. 22. The optical depth to GSC5249-01240 measured by the HST Faint Object Spectrograph on November 21–22, 1995, as this $M_B = 12.2$ star was occulted by material in the D ring. The instrumental noise level (based on the standard deviation of measurements below 73,000 km) is illustrated with the error bar at top left. Between 73,200 and 74,000 km, a series of regularly spaced spikes appear at 2–3 σ above the noise. Figure based on data from Bosh et al. (in preparation).

Fig. 22). These spikes in optical depth are almost certainly related to the 30-km structures observed by Cassini. However, the spikes in the occultation data are spaced by roughly 60 km, about twice the interval between the bright peaks measured by Cassini.

To better quantify the observed temporal variability of this region, we computed the effective wavelength of the periodic structure in the Cassini profiles and the HST occultation by first high-pass filtering the profiles to remove the background variations and then finding the peak of the Fourier power spectrum. The derived wavelengths are provided in Table 2, and Fig. 23 illustrates how the apparent wavenumber $k = 2\pi/\lambda$ has changed with time. Note that not only has the measured wavenumber doubled between 1995 and the Cassini epoch, but there is also a detectable trend among the Cassini observations themselves. The single Cassini observation for 2004 yields a wavelength $\lambda = 34.0 \pm 0.4$ km, while the observations taken during the first half of 2005 have an average wavelength of 32.1 ± 0.1 km, the observations taken during late 2005 and early 2006 have an average wavelength of 31.7 ± 0.2 km, and the observations from late 2006 have a wavelength of 30.6 ± 0.1 km. The decreasing wavelength and increasing wavenumber of this structure therefore appears to be an ongoing phenomenon.

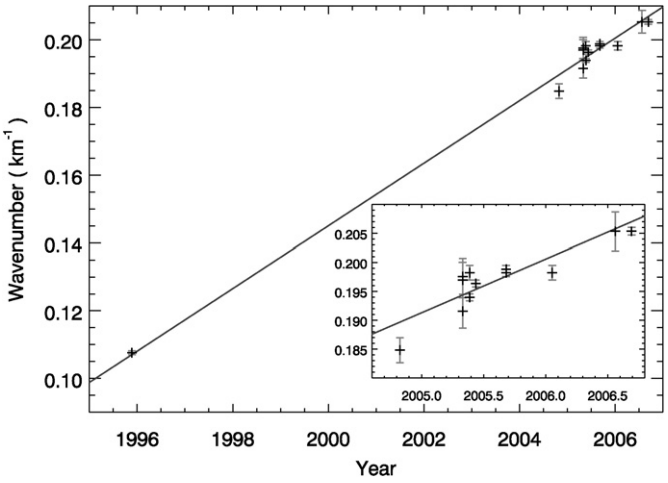

Fig. 23. The measured radial wavenumber $k = 2\pi/\lambda$ of the 30-km structure as a function of time, with an inset showing the Cassini data on a finer scale. Error bars are based on the resolution of the scans. The line corresponds to a steady increase in wavenumber at a rate of 2.5×10^{-5} km^{-1} per day.

Before considering this temporal variability in more detail, we note that the Cassini data also show a finite scatter in wavelength around the mean trend. In particular, the observations taken around days 120 and 140 of 2005 yield wavelengths which vary by about 1 km. These differences are significant. For example, consider the third and fourth profiles in Fig. 17, which were both taken on day 120. The brightness variations in the two profiles are nearly in phase around 73,400 km but are almost 180° out of phase around 73,900 km, which can only happen if the two patterns have different wavelengths. At present, we are unable to fully explain these synchronic wavelength variations. However, for the observations between days 120 and 140, the wavelength appears to be correlated with the scan's longitude relative to the spacecraft, such that scans taken further from the ansa yield slightly longer wavelengths. This may imply that the geometry of observation has some influence on the observed wavelength, although at present we have not yet found any reason why this would be the case.

Even with the finite scatter among the Cassini measurements, we can still use the large time baseline between the HST and Cassini data to estimate how fast the wavelength of the periodic structure changes with time. The most straightforward interpretation of the observed increase in the radial wavenumber is that the periodic structure is a spiral pattern that is winding up over time. If the winding pattern at any given semi-major axis a rotates at a speed Ω_P, then the time derivative of k equals the derivative of Ω_P with respect to a:

$$\frac{\mathrm{d}k}{\mathrm{d}t} = \left|\frac{\mathrm{d}\Omega_P}{\mathrm{d}a}\right|. \tag{9}$$

In this case, $\mathrm{d}k/\mathrm{d}t$ is constant, so the wavenumber k increases linearly with time. Assuming a linear relationship, a least-squares fit of the data yields a slope $\mathrm{d}k/\mathrm{d}t = (2.51 \pm 0.02) \times 10^{-5}$ km^{-1}/day. (Note that in order to avoid giving

Table 2
Wavelengths of ∼30-km structures

Image name	Observation time	Emission angle	Inertial[a] longitude	Apparent[b] longitude	Resolution[c] (km/pix)	Wavelength[d] (km)	Error[e] (km)	Spread[f] (km)
1995 Occultation	1995-325T09:04	87.4	–	–	4.7	58.4	0.3	1.4
N1477594923	2004-301T18:37	81.6	245	64	7.5	34.0	0.4	0.5
N1493537519	2005-120T07:04	109.1	218	87	9.4	31.9	0.5	0.8
N1493557225	2005-120T12:33	109.5	56	−78	8.9	32.8	0.5	1.0
N1493559711	2005-120T13:15	109.5	219	86	8.8	31.8	0.5	0.8
N1495302191	2005-140T17:15	110.7	268	88	3.2	31.7	0.2	0.7
N1495333419	2005-141T01:56	99.3	298	69	1.6	32.5	0.1	0.7
N1496893302	2005-159T03:11	106.7	283	79	2.2	32.0	0.1	0.7
N1504582470	2005-248T03:06	105.9	252	78	2.4	31.6	0.1	0.5
N1504584655	2005-248T03:43	105.8	100	−77	2.3	31.7	0.1	0.6
N1516295176[g]	2006-018T16:37	89.7	286	90[h]	3.8	31.6	0.2	0.7
N1516295866[g]	2006-018T16:48	89.7	97	−90[h]	3.8	31.6	0.2	0.9
N1516322203[g]	2006-019T00:07	89.7	291	90[h]	4.3	31.7	0.3	0.7
N1516322893[g]	2006-019T00:19	89.7	104	−90[h]	4.3	31.7	0.3	0.9
N1516324453[g]	2006-019T00:45	89.7	104	−90[h]	4.3	31.6	0.3	0.8
N1516325158[g]	2006-019T00:56	89.7	292	90[h]	4.3	31.8	0.3	0.7
N1532375310[i]	2006-204T19:17	104.9	75	−76	1.6	30.6[i]	0.5[i]	0.2[i]
N1536502354	2006-252T13:41	118.2	72	−50	1.4	30.6	0.1	0.8

[a] Inertial longitude in Saturn's equatorial plane measured counterclockwise from the north relative to its ascending node on the J2000 equator.
[b] Longitude of scan relative to spacecraft's longitude; ±90 corresponds to the ansae of the rings.
[c] Image pixel scale.
[d] Wavelength of 30-km structure measured between radii of 73,200 and 74,000 km, derived from the peak's location in the Fourier transform (see text).
[e] The error on estimated wavelength, calculated from the image resolution (error $= \sqrt{2}\lambda \times$ (resolution/800 km)).
[f] Width of the peak in the Fourier transform. The spread exceeds the error because there is slight increase in wavelength with radius.
[g] For these images, wavelengths, errors and spreads were estimated using three columns in each image, each of which provides a high-resolution radial scan. The values reported are the means of the three scans for each image.
[h] Due to low opening angles, the values given here are only approximate.
[i] This is a high-resolution image of the outer D ring which only covered the region exterior to 73,600 km. The wavelength of the 30-km structure was therefore computed using only the region between 73,700 and 74,000 km. This estimate of the wavelength was 31.7 km, but since the wavelength of this structure increases with radius we must scale this number to estimate of the average wavelength for the entire range 73,200 and 74,000 km. Comparing the measured wavelengths between 73,200 and 74,000 km and between 73,700 and 74,000 km for the four scans from 2005 with resolutions better than 3 km/pixel, we estimate that the scaling factor is 0.967 ± 0.015 (the high-resolution scan in 2006 has a lower signal-to-noise in the region between 73,700 and 74,000 km and therefore was not included in this calculation). The wavelength presented for this scan is scaled by this factor, while the error is dominated by the uncertainty in the correction factor. The spread is small for this observation because of the narrower range of radii considered.

undue weight to the six high-phase images taken on day 18 of 2006, the fit uses a single typical value of the six wavelengths from the set.)

We can now compare the observed winding rate with the predicted winding rates for different spiral patterns having different speeds Ω_P. For example, say the pattern was produced by a narrow band of material winding up due to Keplerian shear, like structures recently observed in the F ring (Charnoz et al., 2005). In that case, the spiral pattern at any semi-major axis moves at the local orbital rate, so $\Omega_P = n \simeq \sqrt{GM/a^3}$, in which case $\mathrm{d}k/\mathrm{d}t \simeq 3/2\sqrt{GM/a^5} = 54 \times 10^{-5}$ km^{-1}/day for $a = 73{,}600$ km. This is over twenty times the observed rate. The regular structure is therefore winding up much too slowly to be a simple Keplerian spiral.

As we have seen, the apparent brightness variations can be interpreted as vertical corrugations in the ring, which leads us to consider the nodal regression rate $n - \nu$, which to first order is $-3/2\sqrt{GM/a^3}J_2(R_P/a)^2$, where $R_P = 60{,}330$ km and $J_2 = (16290.71 \pm 0.27) \times 10^{-6}$ (Jacobson et al., 2006) represents Saturn's oblateness. At this level of approximation,

$$\mathrm{d}k/\mathrm{d}t \simeq (21/4)J_2\sqrt{GM/a^5}(R_P/a)^2. \quad (10)$$

Assuming $a \simeq 73{,}600$ km, we find that differential regression gives a winding rate of 2.0×10^{-5} km^{-1}/day, which is much closer to the observed rate. If we include the higher-order gravity harmonics $J_4 = (-936 \pm 3) \times 10^{-6}$ and $J_6 = (86 \pm 10) \times 10^{-6}$ (Jacobson et al., 2006) in the calculation, we obtain a winding rate of $\mathrm{d}k/\mathrm{d}t = (2.38 \pm 0.01) \times 10^{-5}$ km^{-1}/day, less than 10% from the observed rate. The steady decrease in the wavelength of the periodic structure in the outer D ring is therefore consistent with it being due to differential precession of an initially inclined ring, which slowly crumples into a tighter and tighter spiral. This lends further support to our model of the periodic brightness variations being due to vertical corrugations, and not due to a series of discrete ringlets, whose spacings would likely evolve at a much slower rate due to non-gravitational forces.

Note that both because $(R_P/a)^2 \simeq 0.67$ is not much less than unity in this part of the D ring, and because the winding rate scales like the derivative of the precession rate, $\mathrm{d}k/\mathrm{d}t$ is very sensitive to higher-order gravity harmonics including J_8 through J_{14}, which are not yet well constrained by the spacecraft trajectory, etc. This could account for part of the difference between the calculated and measured winding rates. Further-

more, refined measurements of the winding rate as a function of orbital position that properly account for image projection effects, combined with data from other eccentric features in the inner ring system (cf. Nicholson and Porco, 1988) and from the spacecraft trajectory, have the potential to help provide very stringent constraints on Saturn interior models.

Additional evidence that the regular structure in the outer D ring results from a winding vertical corrugation can be found using the observed trends in the pattern's wavelength with radius. Differential precession should cause the wavelength around 73,900 km to be about 5% longer than the wavelength at 73,400 km. While such a small shift in wavelength cannot be discerned with confidence in any single profile, if we measure the ratio of wavelengths measured around 73,400 and 73,900 km in all the Cassini profiles, we find the average wavelength in the exterior region is $5 \pm 3\%$ longer than that of the interior region, consistent with the prediction. This conclusion will be strengthened as Cassini returns new data.

This model for the regular structure around D73 also makes some very definite predictions for the future of the outer D ring. The pattern's wavelength should continue to systematically decrease over time. However, when the wavelength of the corrugations becomes comparable to the thickness of the disk, collisions between ring particles will finally damp out the inclinations and bring all the material down into the equatorial plane. At this time, the photometric properties of the ring may change dramatically. Additional observations and modeling of the available data should allow us to understand when this transition is likely to occur.

6.3. The origin of the regular structure: An impact?

The above data provide good evidence that the outer D ring is vertically corrugated with a typical wavelength today of ~30 km and an amplitude of ~1 km. The comparison with HST data also indicates that this corrugation is really a spiral pattern, with the radial spacing between adjacent crests of the spiral progressively declining over time due to differential regression of the nodes. If we fit the data in Fig. 23 to a line and extrapolate backwards in time, we find $k = 0$ on day 130 of 1984 with an uncertainty of ± 50 days. At this time, an inclined sheet of material would have extended between 73,200 and 74,000 km (although the inclination likely varied with radius), implying that some torque had acted on the material in this region and tilted its mean angular momentum vector out of alignment with the rest of the ring system. At present we do not have a complete explanation for what happened to the D ring in 1984, but in order to lay the groundwork for future research on this subject, we here speculate about the possibility that a comet or meteoroid may have collided with the inner ring system.

An impact event could carry sufficient angular momentum into the D ring to produce a detectable change in its inclination. The total mass of a ring at orbital radius r and width δr is

$$M \simeq (4/3)\pi r \delta r \tau \rho d_P, \tag{11}$$

where τ is the normal optical depth of the ring, ρ is the mass density of the ring particles and d_P is the mean diameter of the ring particles. The HST occultation data indicates that $\tau \sim 10^{-3}$ (Bosh and Olkin, 1996), and we will assume that the D-ring particles have a typical size of 10 microns and are composed primarily of water ice ($\rho = 0.92$ g/cm^3), consistent with the Cassini photometric and spectroscopic data. In this case, the total mass in the region between 73,200 and 74,000 km is of order 2×10^9 kg, equivalent to a solid object 150 m in diameter. In order for an ice-rich impactor to have sufficient momentum to produce a mean inclination of 10^{-5} in this quantity of material, assuming it approached the ring face-on with a typical velocity of 40 km/s, it would have to have a mass of order 12,500 kg and thus be a few meters across. The flux of meter-sized bodies into the rings is highly uncertain, but assuming a flux of 10^{-21}–10^{-22}/m^2/s consistent with extrapolations of the flux distributions from Ip (1984) and Cuzzi and Estrada (1998), we find that about 1–10 such objects pass through the D ring per year. Of course, for the impactor to transfer sufficient angular momentum to the D-ring material, it would have to collide with a comparably massive object orbiting in the ringplane, and the number density of suitably large particles in the D ring is unknown. However, we can estimate a maximum collision rate by assuming the entire optical depth of the D ring (10^{-3} from Bosh and Olkin, 1996) is composed of large particles, in which case the collision rate would be between one per century and one per millennium. We also note that if the impactor collided with a body in the ring that was already on an inclined orbit due to an interaction with a vertical resonance, the required mass of the impactor could be reduced, increasing the potential collision rate. In any case, the probability of a suitably large impact into the D ring occurring in the last quarter-century is not vanishingly small.

An impact event would release a cloud of small particles with a range of inclinations and eccentricities into the D ring. The scattered particles would then collide with each other and with other particles in the D ring, and these collisions should damp the relative inclinations and eccentricities. Detailed numerical modeling will likely be necessary before we can determine whether the particles released from a suitable collision can yield a warped ring consistent with our observations. Since such a model is beyond the scope of this paper, we present here some simple considerations which demonstrate that this idea is worth further investigation.

The collisional damping time scale for a ring of material $T_D \sim P/2\tau$, where P is the orbital period of the material (Burns et al., 1984). From the HST data, we know $\tau \sim 10^{-3}$ (Bosh and Olkin, 1996), and in the D ring $P \sim$ a few hours, so T_D is less than a year. We therefore expect that within a couple of years of the impact the D ring would have collapsed so that at each radius the particles were all on nearly circular orbits with nearly the same inclination. However, this inclination need not have been zero. Since the impactor struck the ring from one side and in one place, the particles ejected from the collision would have had their nodes aligned at similar inertial longitudes, in which case the ring could have collapsed into a thin disk with finite inclination. The ring will only collapse into Saturn's equatorial plane if differential nodal regression destroys the alignment of the nodes over a zone where particles are likely

to interact and collide. From the above discussion of winding rates, we know the differential regression rate in this region is about 2.5×10^{-5} km^{-1}/day. Assuming the initial eccentricities were comparable to the present inclinations of 10^{-5}, the interaction zone for a particle would be ~1 km across and it would take over 100 years for the differential nodal regression of interacting particles to develop substantially different nodes. Of course, the eccentricities of the ring particles immediately after the impact may have been somewhat higher than at present, allowing for wider interaction zones, but even after increasing the interaction zone by an order of magnitude, the regression rate will still only produce significant changes in node alignment across the zone in 15 years. Thus it appears that collisional damping is significantly faster than the nodal regression, so the D ring after a collision would probably not produce an equatorial ring, but one that has a finite inclination. Afterwords, the differential regression of the nodes will cause the nodal line to become an increasingly tightly wound spiral. This in turn generates the corrugated ring that was seen by HST in 1995 and now by Cassini.

(We may note that a similar argument could be applied to produce a ring where all the particles are on eccentric orbits with similar pericenters. However, maintaining eccentricities should be more difficult owing to the higher in-plane optical depth and collision frequencies. We also note that eccentricities would not produce the observed contrast reversals so naturally.)

Future work will focus on developing more sophisticated analytical and numerical models to determine if a group of particles released in a collision within an existing low-optical-depth ring will yield a warped ring with the appropriate characteristics. In particular, it is not obvious at present if a single collision can affect the inclination of material spread across 800 km in semi-major axis.

7. Dynamical considerations for other parts of the D ring

While we have a rough model of the regular structure outside D73, many other features of the D ring have not yet been explained, including the sorting of material around 73,450 and 73,700 km, the apparent radial excursions of D68, and the changes and structures seen in and around D72. In order to help other researchers to develop and test possible explanations for these structures, we collect here some basic facts about the dynamical environment of the D ring.

The orbital periods of D-ring particles range from 5.25 h to nearly 6 h. Owing to the D-ring's proximity to Saturn with its substantial oblateness, orbital pericenters precess and nodes regress over the course of about a week. The fundamental planetary spin period remains somewhat uncertain (Sánchez-Lavega, 2005; Giampieri et al., 2006) but is 10.7–10.8 h, so that one-half of it is 5.38 h. This region therefore contains resonances with the planet's free-oscillation modes (Marley and Porco, 1993) and with the periodic Lorentz forces on charged grains (Burns et al., 2001; Hamilton, 1994).

The orbital periods of a few satellites are simple multiples of the orbital periods of ring material: one-fourth of Mimas' period is 5.65 h and one-third of Janus/Epimetheus' is 5.56 h. The fact that many of these periods are commensurable encourages the hope that resonances may be involved in some D-ring structures. Moreover, resonant locations, especially of higher-order resonances, are widely separated owing to Saturn's substantial oblateness. For example, using the expressions found in Murray and Dermott (1999, Appendix B.16) and current values for J_2 and J_4, we find that Mimas' various 4:1 inclination resonances are located at 72,220, 73,111, 73,124, 73,949, 73,962 and 74,754 km (Porco et al., 2006, in preparation).

Many particles comprising the D ring are small enough that they are susceptible to radiation forces (Burns et al., 2001). However, since the local environment has not been directly sampled, we are unable to estimate timescales for orbital evolution by exospheric drag, plasma drag or resonant charge variations, but we anticipate that such drag forces will all induce rapid orbital decay, significantly accelerating the collapse that would occur under Poynting–Robertson drag alone. The latter timescale is estimated to be 10^5 years for micron-sized grains (Burns et al., 2001). Lifetimes due to sputtering and micrometeoroid bombardment are likely to be shorter, perhaps a thousand years, but are very uncertain because the bombarding flux in this region is poorly known. The former process would be driven by energetic particles from Saturn's inner radiation belt, discovered by Cassini (Krimigis et al., 2005).

8. Conclusions

In Cassini's first two years of observations, Saturn's D ring has been found to contain many complex and dynamic features that were not visible in Voyager's few images. Among the surprises are significant secular changes in D72's position and brightness over the last twenty-five years, apparent radial excursions of the narrow ringlet D68, and quasi-regular undulations exterior to D73. This low-optical-depth ring resides in a unique dynamical regime very close to the planet, where tidal forces, high-order gravitational harmonics and electromagnetic effects may all be important. Thus, if we are able to uncover the processes responsible for creating these striking structures, we will likely gain new insights into ring dynamics in general.

Additional observations of the D-ring region to be obtained by Cassini at different times and in various geometries should help to clarify the nature of these features, and confirm whether our model for the regular structure is correct. Moreover, ongoing studies of the photometry and spectra of these features should provide further clues about the compositions and size distribution of the constituent particles. Hopefully all of this information will enable us, or others, to make sense of this puzzling ring.

Acknowledgments

We hereby acknowledge the support of the Cassini imaging team, the VIMS team, the Cassini Project and NASA's, PG&G program. We thank the staff within CICLOPS at the Space Science Institute for planning many of the images, the VIMS support team for their role in acquiring the VIMS data, and M.W. Evans for helping with software development. We

also thank C.D. Murray, J.N. Cuzzi, H. Throop, and one anonymous reviewer for their helpful comments.

References

Bosh, A.S., Olkin, C.B., 1996. Low optical depth features in Saturn's rings: The occultation of GSC5249-01240 by Saturn and its rings. Bull. Am. Astron. Soc. 28, 1124.

Bosh, A.S., Olkin, C.B., French, R.G., Nicholson, P.D., 2002. Saturn's F ring: Kinematics and particle sizes from stellar occultation studies. Icarus 157, 57–75.

Brown, R.H., Baines, K.H., Bellucci, G., Bibring, J.-P., Buratti, B.J., Capaccioni, F., Cerroni, P., Clark, R.N., Coradini, A., Cruikshank, D.P., Drossart, P., Formisano, V., Jaumann, R., Langevin, Y., Matson, D.L., McCord, T.B., Mennella, V., Miller, E., Nelson, R.M., Nicholson, P.D., Sicardy, B., Sotin, C., 2004. The Cassini Visual and Infrared Mapping Spectrometer (VIMS) investigation. Space Sci. Rev. 115, 111–168.

Burns, J.A., Hamilton, D.P., Showalter, M.R., 2001. Dusty rings and circumplanetary dust: Observations and simple physics. In: Grun, E., Gustafson, B., Dermott, S., Fechtig, H. (Eds.), Interplanetary Dust. Springer-Verlag, Berlin, pp. 641–725.

Burns, J.A., Showalter, M.R., Morfill, G.E., 1984. The ethereal rings of Jupiter and Saturn. In: Greenberg, R., Brahic, A. (Eds.), Planetary Rings. Univ. of Arizona Press, Tucson, pp. 200–272.

Charnoz, S., Porco, C.C., Déau, E., Brahic, A., Spitale, J.N., Bacques, G., Baillie, K., 2005. Cassini discovers a kinematic spiral ring around Saturn. Science 310, 1300–1304.

Cuzzi, J.N., Estrada, P.R., 1998. Compositional evolution of Saturn's rings due to meteoroid bombardment. Icarus 132, 1–35.

French, R.G., Nicholson, P.D., Cooke, M.L., Elliot, J.L., Matthews, K., Perkovic, O., Tollestrup, E., Harvey, P., Chanover, N.J., Clark, M.A., Dunham, E.W., Forrest, W., Harrington, J., Pipher, J., Brahic, A., Grenier, I., Roques, F., Arndt, M., 1993. Geometry of the Saturn system from the 3 July 1989 occultation of 28 SGR and Voyager observations. Icarus 103, 163–214.

French, R.G., Nicholson, P.D., Porco, C.C., Marouf, E.A., 1991. Dynamics and structure of the uranian rings. In: Bergstralh, J.T., Miner, E.D., Matthews, M.S. (Eds.), Uranus. Univ. of Arizona Press, Tucson, pp. 327–409.

Gehrels, T., Baker, L.R., Beshore, E., Blenman, C., Burke, J.J., Castillo, N.D., Dacosta, B., Degewij, J., Doose, L.R., Fountain, J.W., Gotobed, J., Kenknight, C.E., Kingston, R., McLaughlin, G., McMillan, R., Murphy, R., Smith, P.H., Stoll, C.P., Strickland, R.N., Tomasko, M.G., Wijesinghe, M.P., Coffeen, D.L., Esposito, L.W., 1980. Imaging photopolarimeter on Pioneer Saturn. Science 207, 434–439.

Giampieri, G., Dougherty, M.K., Smith, E.J., Russell, C.T., 2006. A regular period for Saturn's magnetic field that may track its internal rotation. Nature 441, 62–64.

Gresh, D.L., Rosen, P.A., Tyler, G.L., Lissauer, J.J., 1986. An analysis of bending waves in Saturn's rings using Voyager radio occultation data. Icarus 68, 481–502.

Guérin, P., 1973. Les anneaux de Saturne en 1969. Etude morphologique et photométrique. I. Obtention et dépouillement des photographies. Icarus 19, 202–211.

Hamilton, D.P., 1994. A comparison of Lorentz, planetary gravitational, and satellite gravitational resonances. Icarus 109, 221–240.

Ip, W.-H., 1984. Ring torque of Saturn from interplanetary meteoroid impact. Icarus 60, 547–552.

Jacobson, R.A., Antreasain, P.G., Bordi, J.J., Criddle, K.E., Ionasescu, R., Jones, J.B., Mackenzie, R.A., Meek, M.C., Parcher, D., Pelletier, F.J., Owen Jr., W.M., Roth, D.C., Roundhill, I.M., Stauch, J.R., 2006. The gravity field of the saturnian system from satellite observations and spacecraft tracking data. Astron. J. 132, 2520–2526.

Krimigis, S.M., Mitchell, D.G., Hamilton, D.C., Krupp, N., Livi, S., Roelof, E.C., Dandouras, J., Armstrong, T.P., Mauk, B.H., Paranicas, C., Brandt, P.C., Bolton, S., Cheng, A.F., Choo, T., Gloeckler, G., Hayes, J., Hsieh, K.C., Ip, W.-H., Jaskulek, S., Keath, E.P., Kirsch, E., Kusterer, M., Lagg, A., Lanzerotti, L.J., LaVallee, D., Manweiler, J., McEntire, R.W., Rasmuss, W., Saur, J., Turner, F.S., Williams, D.J., Woch, J., 2005. Dynamics of Saturn's magnetosphere from MIMI during Cassini's orbital insertion. Science 307, 1270–1273.

Marley, M.S., Porco, C.C., 1993. Planetary acoustic mode seismology—Saturn's rings. Icarus 106, 508–524.

McCord, T.B., Coradini, A., Hibbitts, C.A., Capaccioni, F., Hansen, G.B., Filacchione, G., Clark, R.N., Cerroni, P., Brown, R.H., Baines, K.H., Bellucci, G., Bibring, J.-P., Buratti, B.J., Bussoletti, E., Combes, M., Cruikshank, D.P., Drossart, P., Formisano, V., Jaumann, R., Langevin, Y., Matson, D.L., Nelson, R.M., Nicholson, P.D., Sicardy, B., Sotin, C., 2004. Cassini VIMS observations of the Galilean satellites including the VIMS calibration procedure. Icarus 172, 104–126.

Murray, C.D., Dermott, S.F., 1999. Solar System Dynamics. Cambridge Univ. Press, Cambridge, UK.

Nicholson, P.D., Porco, C.C., 1988. A new constraint on Saturn's zonal gravity harmonics from Voyager observations of an eccentric ringlet. J. Geophys. Res. 93, 10209–10224.

Ockert-Bell, M.E., Burns, J.A., Daubar, I.J., Thomas, P.C., Veverka, J., Belton, M.J.S., Klaasen, K.P., 1999. The structure of Jupiter's ring system as revealed by the Galileo imaging experiment. Icarus 138, 188–213.

Pollack, J.B., Cuzzi, J.N., 1980. Scattering by non-spherical particles of size comparable to wavelength—A new semi-empirical theory and its application to tropospheric aerosols. J. Atmos. Sci. 37, 868–881.

Porco, C.C., Baker, E., Barbara, J., Beurle, K., Brahic, A., Burns, J.A., Charnoz, S., Cooper, N., Dawson, D.D., Delgenio, A.D., Denk, T., Dones, L., Dyudina, U., Evans, M.W., Giese, B., Grazier, K., Helfenstein, P., Ingersoll, A.P., Jacobson, R.A., Johnson, T.V., McEwen, A., Murray, C.D., Neukum, G., Owen, W.M., Perry, J., Roatsch, T., Spitale, J., Squyres, S., Thomas, P., Tiscareno, M., Turtle, E., Vasavada, A.R., Veverka, J., Wagner, R., West, R., 2005. Cassini Imaging Science: Initial results on Saturn's rings and small satellites. Science 307, 1226–1236.

Porco, C.C., West, R.A., Squyres, S., McEwen, A., Thomas, P., Murray, C.D., Delgenio, A., Ingersoll, A.P., Johnson, T.V., Neukum, G., Veverka, J., Dones, L., Brahic, A., Burns, J.A., Haemmerle, V., Knowles, B., Dawson, D., Roatsch, T., Beurle, K., Owen, W., 2004. Cassini Imaging Science: Instrument characteristics and anticipated scientific investigations at Saturn. Space Sci. Rev. 115, 363–497.

Sánchez-Lavega, A., 2005. How long is the day on Saturn? Science 307, 1223–1224.

Showalter, M.R., 1996. Saturn's D ring in the Voyager images. Icarus 124, 677–689.

Showalter, M.R., Cuzzi, J.N., Marouf, E.A., Esposito, L.W., 1986. Satellite "wakes" and the orbit of the Encke Gap moonlet. Icarus 66, 297–323.

Showalter, M.R., Hamilton, D.P., Burns, J.A., de Pater, I., Simonelli, D.P., 2001. Structure of Jupiter's main ring and halo from Galileo SSI and Earth-based images. In: Bagenal, F. (Ed.), Conference "Jupiter: Planet, Satellites and Magnetosphere," Boulder, CO, June 25–30. LASP, pp. 101–102.

Showalter, M.R., Pollack, J.B., Ockert, M.E., Doyle, L.R., Dalton, J.B., 1992. A photometric study of Saturn's F ring. Icarus 100, 394–411.